1-1-2010

Imaging The Vasculature With Susceptibility Weighted Imaging: Applications And Analysis

Samuel Barnes
Wayne State University

Recommended Citation
Barnes, Samuel, "Imaging The Vasculature With Susceptibility Weighted Imaging: Applications And Analysis" (2010). *Wayne State University Dissertations.* Paper 4.

IMAGING THE VASCULATURE WITH SUSCEPTIBILITY WEIGHTED IMAGING: APPLICATIONS AND ANALYSIS

by

SAMUEL RYAN STURGILL BARNES

DISSERTATION

Submitted to the Graduate School

of Wayne State University,

Detroit, Michigan

in partial fulfillment of the requirements

for the degree of

DOCTOR OF PHILOSOPHY

2010

MAJOR: BIOMEDICAL ENGINEERING

Approved by:

____
Advisor   Date

____

____

____

ACKNOWLEDGEMENTS

I would like to acknowledge my advisor Dr. Haacke for all the help and encouragement over the years, teaching me to think critically and see the big picture. I would also like to thank Muhammad Ayaz, Jaladhar Neelavalli, and Grant McAuley for many helpful discussions and being good sounding boards for ideas. Many thanks to Andy Obenaus for helpful critiques of my presentations and especially my paper figures. I would like to thank Dr. Kido for introducing me to an exciting field and giving good advice about my career, research, and personal life along the way. Finally, I would like to thank my parents and brother for teaching me the value of discipline and hard work that made this all possible.

This research was supported in part by NIH grant NHLBI62983 and by a grant from Siemens Healthcare.

TABLE OF CONTENTS

LIST OF TABLES

CHAPTER 1 – MOTIVATION AND BASIC MAGNETIC RESONANCE IMAGING

Introduction

Modern magnetic resonance imaging (MRI) enables non-invasive imaging of the vasculature in the human body with detail that was previously only available post-mortem or with invasive and ionizing radiation based techniques. The development of magnetic resonance angiography (MRA) in the 1980s (Nayler et al. 1986; Nishimura et al. 1986; Haacke and Lenz 1987) allowed for detailed imaging of the arteries using MR. More recently the development of susceptibility weighted imaging (SWI) (Reichenbach et al. 1997; Haacke et al. 2004) has made very detailed venography (with veins as small as 200-300µm visible) feasible, which has allowed the role of veins in various diseases to be examined in more detail. The availability of safe and detailed vascular information of the arteries and veins has allowed new links to be proposed and discovered between different diseases and the vasculature, from multiple sclerosis (MS) to cancer to Alzheimer’s disease (Ayaz et al. 2009; Bullitt et al. 2009; Ge et al. 2009; Singh and Zamboni 2009).

In this work, we look at different applications of SWI and MRA to image the vasculature throughout the body with two chapters on MR development, one chapter on image analysis, and one chapter on a physiological application. Chapters two and three look at developing improved MR imaging techniques using SWI to image the arteries and veins simultaneously and to acquire higher resolution MRA scans to image small arteries. Chapter four examines how SWI images can be analyzed and quantified with a proposed algorithm for semi-automated identification of cerebral micro bleeds (CMB). Chapter five looks at an application of SWI in the leg where we show it is possible to image blood stasis and settling in the veins of the leg with possible applications to deep venous thrombosis (DVT).

Basic SWI Concepts

The SWI sequence is akin to a standard flow compensated gradient echo sequence (Reichenbach et al. 1997; Haacke et al. 2004). Gradient echo imaging is particularly sensitive to local changes in magnetic field. Specifically, a gradient echo sequence is more sensitive than a spin echo sequence to static local field changes. This variation in magnetic field changes the spin phase over time and so, at longer echoes, the spins dephase causing the magnitude signal to disappear. This additional dephasing that is not present in spin echo scans is referred to as T2´. The total relaxation rate is given by R2* = R2 + R2´ where R2* = 1/T2*, R2 = 1/T2 and R2´ = 1/T2´.

In addition to the T2* weighted magnitude image, SWI uses the phase data to increase the sensitivity to these local field changes. For a right handed system, phase is given by

$$\Delta\varphi = -\gamma \cdot \Delta B \cdot TE \tag{1.1}$$

with γ the gyromagnetic ratio of hydrogen (42.6 MHz/T) and ΔB the local change in magnetic field (which can be caused by local tissue susceptibility changes such as those caused by iron, calcium or other structural effects in the tissue). Although these SWI phase images are of great interest in and of themselves (Haacke et al. 2004; Duyn et al. 2007), the phase can also be combined with the magnitude image using a phase mask (described below) to create a hybrid image. This new image accentuates both the T2* contrast, from the magnitude image, and phase information into a single SW image (Figure 1.1). It is this form of SWI data that has become best known (Haacke et al. 2009; Mittal et al. 2009).

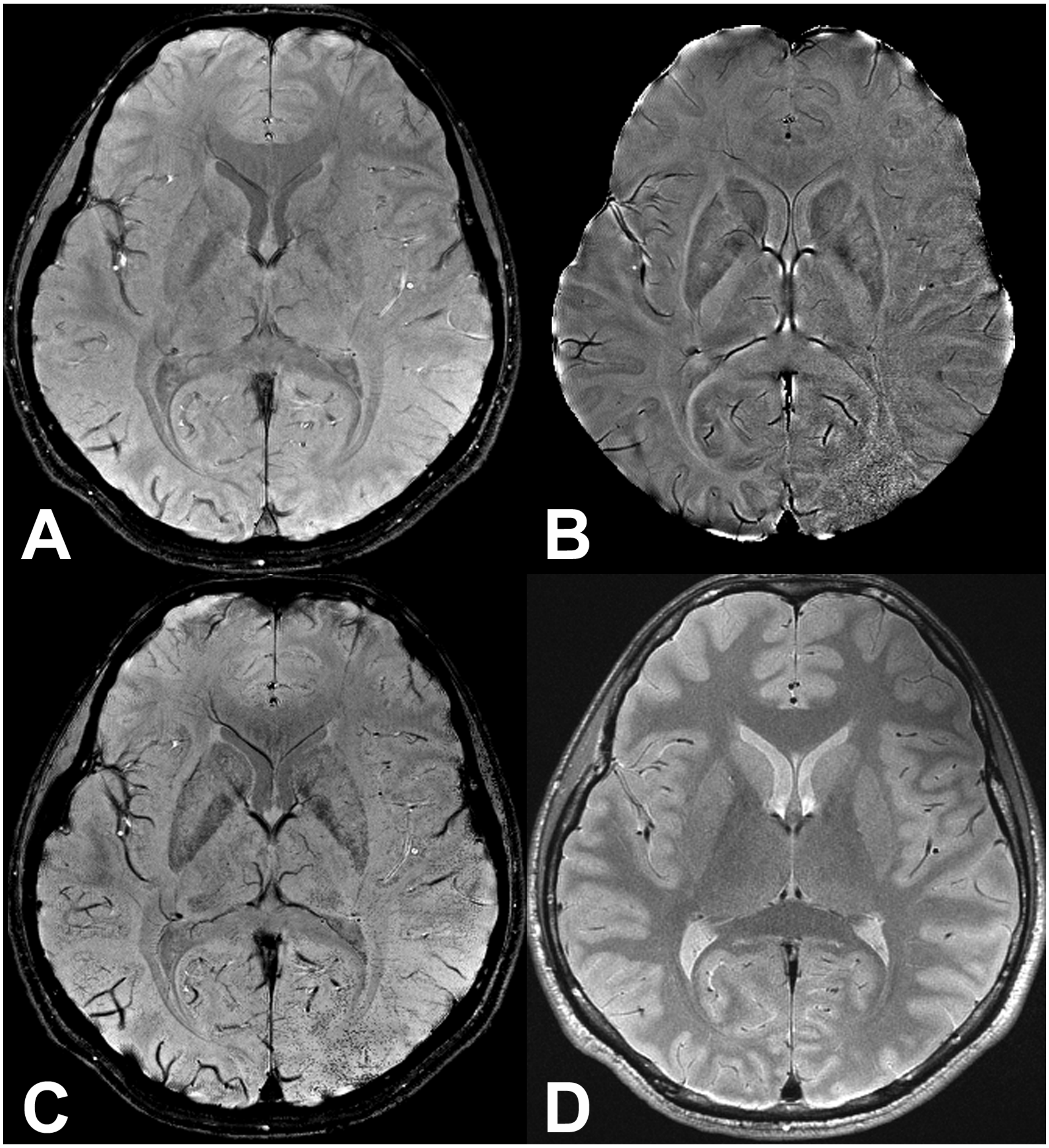

Figure 1.1. Single slice comparing SWI and other images at 4T, A) SWI magnitude image (T2* weighted) B) SWI phase image C) SW Image D) proton density image. Note that the SW image (C) combines features from both the magnitude (A) and phase (B).

SWI data are collected with a long-TE, fully flow-compensated gradient echo scan; this can be in the form of a single-echo, multiple-echo (Du and Jin 2008; Park et al. 2009; Denk and Rauscher 2010) or segmented echo-planar approach (Xu and Haacke 2008). Imaging with long echoes with reasonable signal-to-noise became possible by using 3D gradient echo imaging

(Reichenbach et al. 1997). This allowed for thinner slices (1-2mm) which reduced dephasing across the slice and improved image quality. Flow compensation in all directions is useful in SWI because the long echo times required can cause flow related signal loss without it. Also since phase is being used as a measure of tissue susceptibility, the flow compensation helps reduce confounding phase from flowing blood. Velocity compensation is usually enough to reduce flow related signal loss in the magnitude image, and flow induced changes in the phase image (Haacke et al. 2009).

If one considers two tissues with different susceptibilities $\Delta\chi$, equation 1.1 can be rewritten so changes in the phase image are generated according to the formula

$$\Delta\varphi = -\gamma \cdot \left(\Delta\chi B_0 G + \Delta B_{CS} + \Delta B_{geometry} + \Delta B_{main\,field}\right) \cdot TE \tag{1.2}$$

where G represents a constant dependent on the geometry of the object, ΔB_{CS} refers to chemical shift, $\Delta B_{geometry}$ refers to the geometry of the brain and air/tissue interfaces, and $\Delta B_{main\ field}$ refers to inhomogeneities in the main field. In equation 1.2, we have rewritten $\Delta B = \Delta\chi B_0$ where $\Delta\chi$ represents the local susceptibility change between tissues. The first two terms are of particular interest to us and are meant to represent the local changes in field, such as those that might be caused by iron in tissue. The last two terms represent unwanted field effects and tend to be slowly varying spatial terms and can be mostly removed using a high-pass spatial frequency filter. With this filtering, ideally, we can isolate the first two terms. Both of them lead to similar phase results inside the object of interest and generate desirable tissue contrast. A paramagnetic object (such as iron) causes a local increase in field and therefore a negative phase change relative to surrounding tissues, while a diamagnetic substance (such as calcium) causes a local decrease in field and therefore a positive phase change.

The phase filter is designed as a homodyne filter whereby a low spatial frequency phase image is divided into the original phase to leave behind high spatial frequency phase. The size of the low pass filter N_f x N_f is usually quoted as something like 64 x 64 for example. However, it might make more sense to refer to the size of the smallest object d_f that is basically removed by the filter. This is given by d_f = FOV/N_f where FOV is the field of view of the image. As an example, consider the FOV = 256 voxels and N_f = 64. In this case, d_f = 4 voxels. The implications are that objects greater than or equal to 4 voxels will be suppressed from the filtered phase image. When aliasing is particularly severe, the phase image can be unwrapped, prior to high pass filtering, to improve the results of the filtering (Rauscher et al. 2003). In some cases, it may be possible to directly remove background phase effects caused by the gross geometry ($\Delta B_{geometry}$ in equation 1.2) with minimal filtering. When the geometry and average susceptibility of the object itself (e.g., the brain) and its surroundings (e.g., the sinuses) are roughly known, their magnetic field effects can be calculated using a forward modeling approach (Neelavalli et al. 2009). These calculated phase effects are then divided out from the measured phase image, prior to high-pass filtering, removing many artifacts from $\Delta B_{geometry}$ and leaving the local changes in susceptibility and phase unaltered, improving the results of the filtering. Whichever filtering technique is used, the resultant filtered phase image is used as described below in all subsequent steps and will be referred to as the SWI filtered phase image.

As mentioned above, the phase image can be combined with the magnitude image using a phase mask. This mask must be created from the filtered phase image and then applied to the magnitude image to generate the SWI data. This mask focuses on certain phase values that will enhance the contrast of the original magnitude image. For example, if areas with increased iron are the subject of interest, then the mask is designed to enhance information related to negative phase (in a right handed system) as follows:

$$f(x) = \begin{cases} \frac{\pi+\varphi(x)}{\pi} & for -\pi < \varphi(x) < 0 \\ 1 & otherwise \end{cases} \tag{1.3}$$

where the phase values can range from –π to π, φ(x) is the phase at location x, and f(x) is the phase mask. This phase mask can be multiplied by the original magnitude image an integer *m* number of times to create the SW image:

$$\rho'(x) = f^m(x) \cdot \rho(x) \tag{1.4}$$

where $\rho'(x)$ is the SW image and $\rho(x)$ is the magnitude image. The number of times the mask is applied will change the contrast in the SW image. It has been shown that four multiplications produces good CNR for a wide range of phase values (Haacke et al. 2004). If the aliasing in the phase image has not been fully removed, which is nearly inevitable in the regions near the frontal sinuses, the residual phase artifacts will destroy the existing magnitude contrast in the SW image rather than enhancing it. This can be overcome by improving the phase filtering, using one of the more advanced techniques discussed above, or alternatively not applying the phase mask in those areas to preserve existing magnitude contrast. Problem areas can be identified by calculating the local field gradients; the phase mask can then be adjusted accordingly to remove problem areas with high local field gradients (Jin et al. 2008). This preserves existing magnitude contrast in problem areas while still getting regular SWI contrast in the rest of brain.

Once this SWI data has been created, it is possible to highlight veins by performing a minimum intensity projection (mIP) over a number of slices. This shows venous connectivity in the same way a maximum intensity projection (MIP) shows arterial connectivity in MRA. A disadvantage of using a mIP is that the dark background surrounding the brain will mask out the brain if it is included in the projection. The slice included in the mIP having the smallest visible brain area will dictate how much of the brain is visible in the final projection. This can be problematic at the top and bottom of the brain where the size changes very rapidly. This problem can be partly overcome by using a brain extraction algorithm, such as a complex threshold approach (Pandian et al. 2008), to set the dark regions outside the brain to a value much higher than the brain during the mIP processing and then back to zero afterward.

Clinically, mIPs are usually limited to projections over 4-8mm, although it is certainly possible to project over more slices near the center of the brain or if the background has been removed to get a better visualized of a larger portion of the venous vasculature.

CHAPTER 2 – SIMULTANEOUS SWI AND MRA

Introduction

Magnetic resonance angiography (MRA) has undergone tremendous development since its inception (Nayler et al. 1986; Nishimura et al. 1986; Haacke and Lenz 1987). To image the vessels in the brain at high fields clinically, there is no longer the need to use contrast agents thanks to the increased signal-to-noise at 3T and the rapid scanning that is possible. Conventional time-of-flight (Potchen et al. 1993) with or without magnetization transfer contrast (MTC) can give excellent coverage with high resolution images. Similarly, SWI can be used to create venographic images of vessels as small as 200 to 300 microns (Reichenbach et al. 1997; Haacke et al. 2004). In this chapter, we will discuss the potential to image both arteries and veins in an SWI single echo time-of-flight (TOF) like sequence.

For the last 100 years, the arterial system has played the major role in the study of the brain’s hemodynamics and, from a surgical point of view, in the study and treatment of atherosclerosis. However, the other half of the story is told by the venous system. SWI like blood oxygen level dependent (BOLD) imaging is sensitive to deoxyhemoglobin in the veins and is able to generate exquisite images of the veins in the brain. SWI is also sensitive to non-heme iron in the form of ferritin or hemosiderin as well and can be used to quantify iron (Haacke et al. 2010) along with T2* maps (Gelman et al. 1999). These two features make SWI a powerful means by which to study neurovascular diseases such as cerebral amyloid angiopathy (CAA), multiple sclerosis (MS), stroke, traumatic brain injury (TBI) and tumors (Mittal et al. 2009).

Both SWI and time-of-flight MRA rely on a flow compensated gradient echo sequence. SWI uses a long echo time and MRA uses a very short echo time. This fact enables SWI and MRA sequences to be combined into a single sequence with two echoes. The first echo is optimized for MRA contrast and the second echo is optimized for SWI contrast. One of the problems in implementing a simultaneous MRA and SWI scan occurs in trying to flow compensate all echoes, which takes considerable time. One way around this is to discard the flow compensation in the phase encoding direction for the first echo (MRA contrast), where it is most important to keep the echo time as short as possible. The second or last echo (SWI contrast) should be flow compensated in all directions as one does not want phase from flow to obscure phase from susceptibility. It is fairly easy to accomplish this given the fact that the SWI sequence itself is usually run with a very long echo to enhance phase effects. The real problem lies in the choice of excitation flip angles so as not to over-suppress the cerebrospinal fluid signal (CSF) and maintain good SWI venous contrast inside the CSF in the gray matter, but still get good excitation of the quickly refreshed arterial blood. A contrast agent can be used to enhance results. In this case, the first echo will show excellent arteries and veins while the SWI long echo will still suppress the veins unlike conventional MRA (Lin et al. 1999).

The possibility of using multiple echoes in SWI to achieve different types of contrast was first explored by Du et al. (Du and Jin 2008). They used a flow compensated short echo to achieve time-of-flight MRA contrast, and a second long echo to achieve SWI contrast. In their implementation, the second echo was not flow compensated in the phase encode directions. This was shown to cause some artifacts in the phase image near flowing arteries and Deistung et al. was able to implement a second echo that was fully flow compensated to remove these artifacts (Deistung et al. 2009). The flow compensation was achieved by fully rewinding the phase encode gradients to zero before performing a second flow compensated phase encode for the next echo. Further modifications such as adjusting the k-space ordering to optimize flip angle choice for each type of contrast and using multiple thin slabs have also been proposed (Park et al. 2009). With these techniques it is possible to achieve both a high quality TOF MRA and a SWI in a single scan that takes approximately the same amount of time as either of those run separately.

These two-echo, two-contrast techniques suggest the possibility of using a general flow compensated multi-echo sequence to achieve a variety of contrasts in both magnitude and phase. As discussed above, the short echoes can be used as an MRA and the long echoes for

SWI contrast (Figure 2.1). The echoes in the middle or after the optimal SWI contrast also have some value. The multiple echo data can be used to calculate T2* maps especially in slow flowing vessels such as the veins and sagittal sinus. They can also be useful for various phase filtering techniques. Finally, having a variety of echo times allows the echo with the optimal susceptibility contrast to be used. Shorter echoes are more optimal for hemorrhages that contain lots or iron, while long echoes are more optimal for imaging tiny venules.

We present here a single echo approach to the same problem. A single echo SWI sequence has been optimized to improve arterial contrast without degrading the traditional SWI contrast. This was accomplished by increasing the resolution, reducing the field echo time to reduce flow related losses and using a downsampling procedure to recover lost SWI contrast.

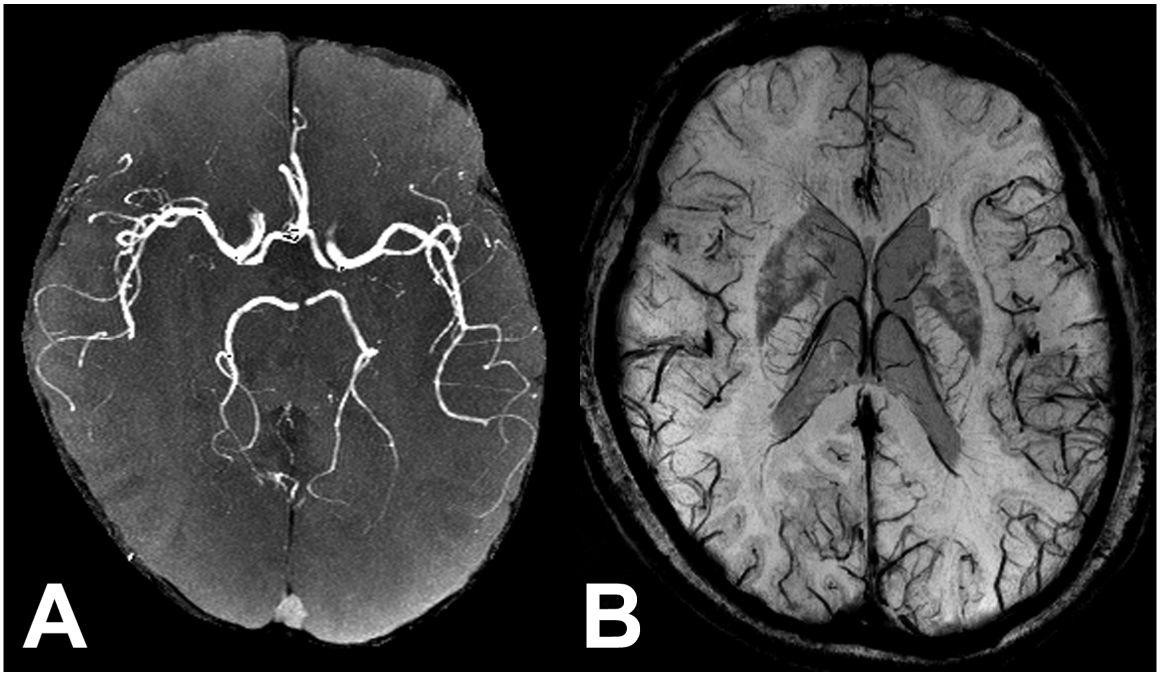

Figure 2.1. A multi-echo SWI sequence with 5 echoes was used to get both MRA and traditional SWI contrast. A) First echo with TE = 6.1ms MIP over 32mm clearly depicts the arteries. B) Fifth echo with TE = 22.1ms mIP over 12mm of SW images shows the veins and traditional SWI contrast.

Single Echo Approach

While the multi-echo approaches can produce excellent angiographic and venographic images, the possibility remains open to achieve similar results with a single echo (Barnes et al. 2010). SWI provides a natural separation of the vasculature, with the arteries being bright from inflow enhancement due to the short TR and the veins dark from the long TE. By using a higher bandwidth and high isotropic resolution to reduce flow dephasing, it is possible to obtain a decent angiogram without significantly degrading the SWI venogram.

Generally, by using a long TE and short TR (typically 20 ms and 30 ms at 3T, respectively) the veins can be suppressed and the arteries brightened, allowing a very good separation of arteries and veins in a single echo scan. The arteries can be visualized using a standard maximum intensity projection (MIP) of magnitude information, and the veins visualized with SWI processing and a minimum intensity projection (mIP). The choice of flip angle, resolution, and echo time is very important for determining image quality of both the MRA and MRV. Higher flip angles improve the angiogram due to increased background suppression and better TOF inflow effect, but in turn degrade the venogram by over-suppressing the CSF. Choosing a medium flip angle (15-20°) and a slightly longer TR appears to be optimal. The longer TR allows more inflow enhancement for the angiography and keeps the CSF from being over-suppressed. Shorter echo times improve the angiography by reducing uncompensated higher-order flow losses, but this decreases venous contrast. At 3T, decreasing the echo time below 20ms substantially degrades venous contrast and is not recommended; an echo time of 20ms is preferred. For this reason, this technique shows promise at higher fields (>3T) as shorter echo times can then be used without degrading venous contrast.

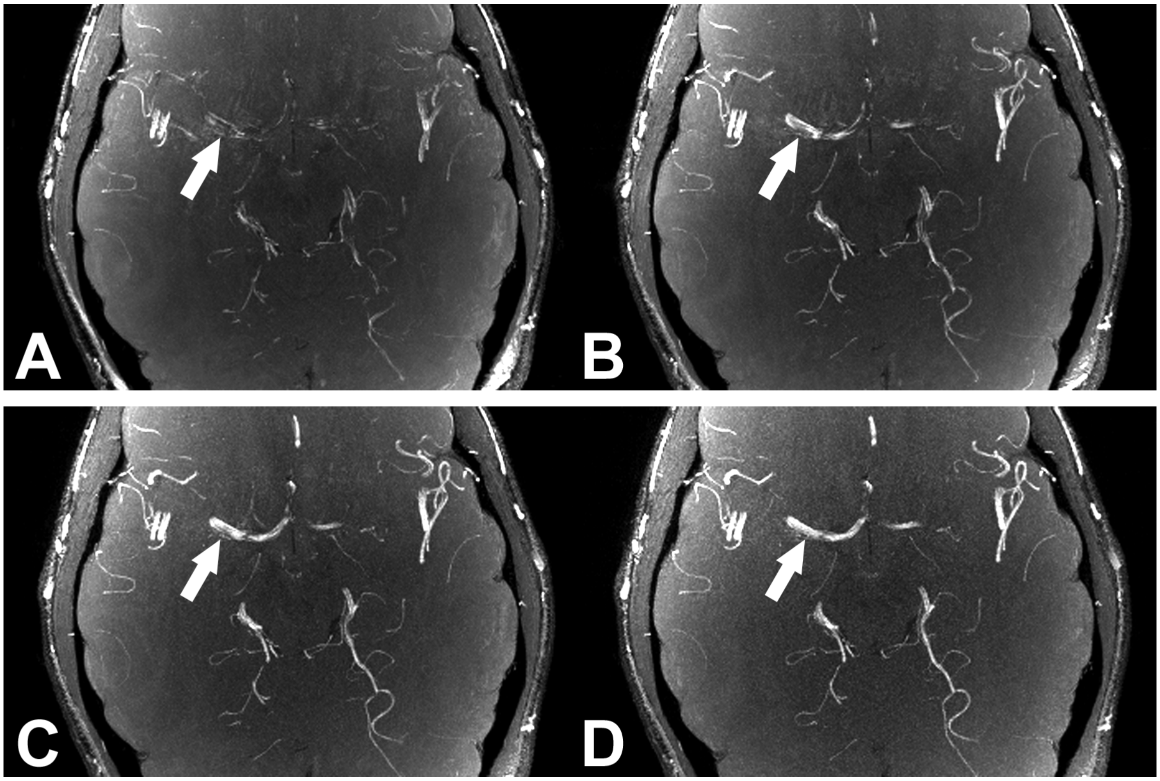

Figure 2.2. MIP images from a long echo scan (20ms) at different bandwidths A) 60 Hz/pixel B) 120 Hz/pixel C) 235 Hz/pixel and D) 465 Hz/pixel. Note that the flow compensation improves at higher bandwidths due to the shortened field echo time as noted by the decreased flow losses in the MCA (arrows).

It is possible to reduce uncompensated higher-order flow losses by increasing the read bandwidth and acquiring the data with high isotropic resolution. A high read bandwidth will reduce the time between spatial encoding and the echo readout; this is referred to as the field echo. Reducing the field echo improves the flow compensation by minimizing higher order flow effects which are proportional to higher powers of the field echo time (Figure 2.2). Keeping the echo time long but reducing the field echo reduces the sensitivity to flow while maintaining T2* contrast. This is only true, however, if you have a homogeneous field. If you have field inhomogeneities, from a poorly shimmed field, air-tissue interfaces, or air-bone interfaces, flow through these inhomogeneities will cause the blood to start developing phase immediately after the excitation pulse, making the flow losses dependant on the echo time, as well as the field echo time. Unfortunately the carotid and parts of the MCA lie in regions of poor field homogeneity due to the sinuses, causing both to experience nearly complete signal loss at long echo times despite very short field echoes. This can be seen in Figure 2.3, where only the part of the MCA that is within the inhomogeneous field (as seen with the phase image) experiences significant signal loss.

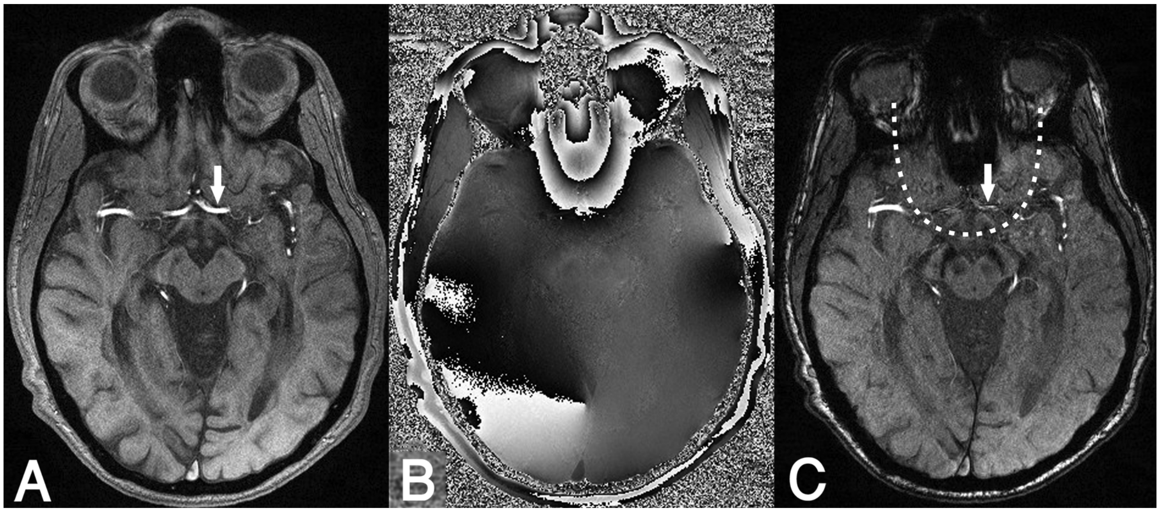

Figure 2.3. A) 7ms magnitude B) 7ms phase C) 24ms magnitude. Notice the more proximal part of the MCA (arrow) that is visible at 7ms is significantly reduced in amplitude at 24ms while the more distal part is still very visible. The proximal part is exposed to field inhomogeneities from the sinuses (indicated with dashed line) causing them to dephase despite the very short field echo time.

High isotropic resolution reduces dephasing across a voxel and thus can reduce flow losses. This does reduce the quality of the SWI phase image as an isotropic aspect ratio of 1:1 in-plane to through-plane resolution is not ideal for SWI (Xu and Haacke 2006; Deistung et al. 2008). The isotropic aspect ratio causes the phase for veins of certain sizes and orientations to have opposite signs (see Figure 2.4). This has the potential to confuse clinical interpretation and could reduce contrast in the SWI processed images. This lost contrast can be completely recovered, however, by post-processing the images and applying a down-sampling filter to generate a more ideal aspect ratio of 1:4. A simple k-space crop can be used, which would be equivalent to a lower resolution acquisition with a 1:4 aspect ratio. Alternatively, a sliding window complex average can be performed, which takes advantage of the fact that the higher resolution was collected. The sliding window filter takes the average of the complex signal (magnitude and phase) over four slices, advances a single slice, calculates the next average, and repeats until all slices are processed. In this way, the through-plane resolution is reduced but the same number of slices as in the original series is maintained (actually the slices will be reduced by a small amount, the collapsing factor minus 1 or three slices in this case).

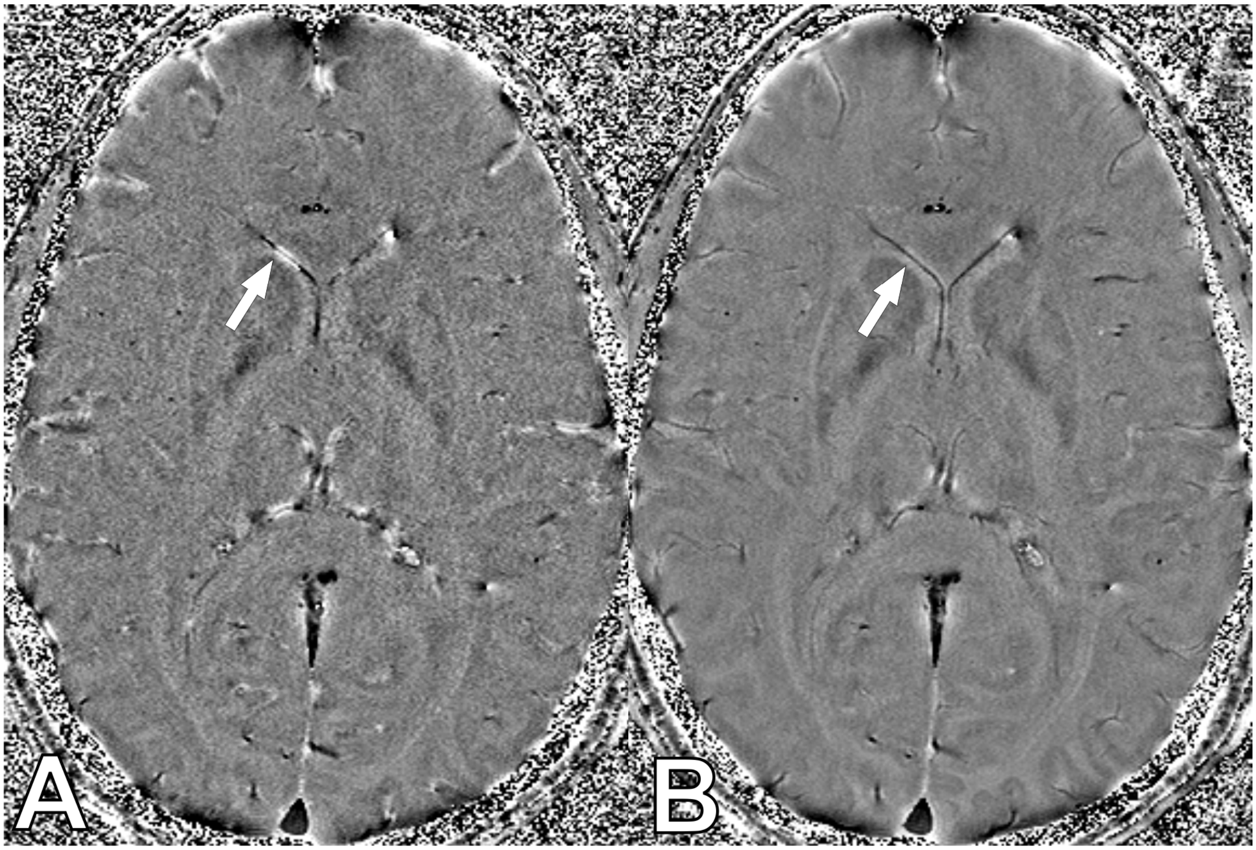

Figure 2.4. A) Isotropic (0.5mm) phase image shows veins switching from bright to dark depending on orientation (arrow). B) Downsampled image shows higher SNR and more homogenous veins (arrow) producing a better venography. The in-plane to through plane aspect ratio of the original image is 1:1 and of the filtered image is 1:4 as in the usual SWI acquisitions. Images acquired at 3T with TE/TR/FA/BW = 20 ms/30 ms/15°/160 Hz/pixel.

By reconstructing the thick slabs in an overlapping pattern, optimal partial voluming of small structures is guaranteed, increasing their visibility (Figure 2.5). This reconstruction also offers a distinct advantage over the original k-space data in that it uses the high-pass filtered phase in the complex downsampling process, and not the original phase. This reduces the dephasing in areas of rapid phase change (air-tissue interfaces), reducing signal loss in the magnitude image and improving the quality of the downsampled images.

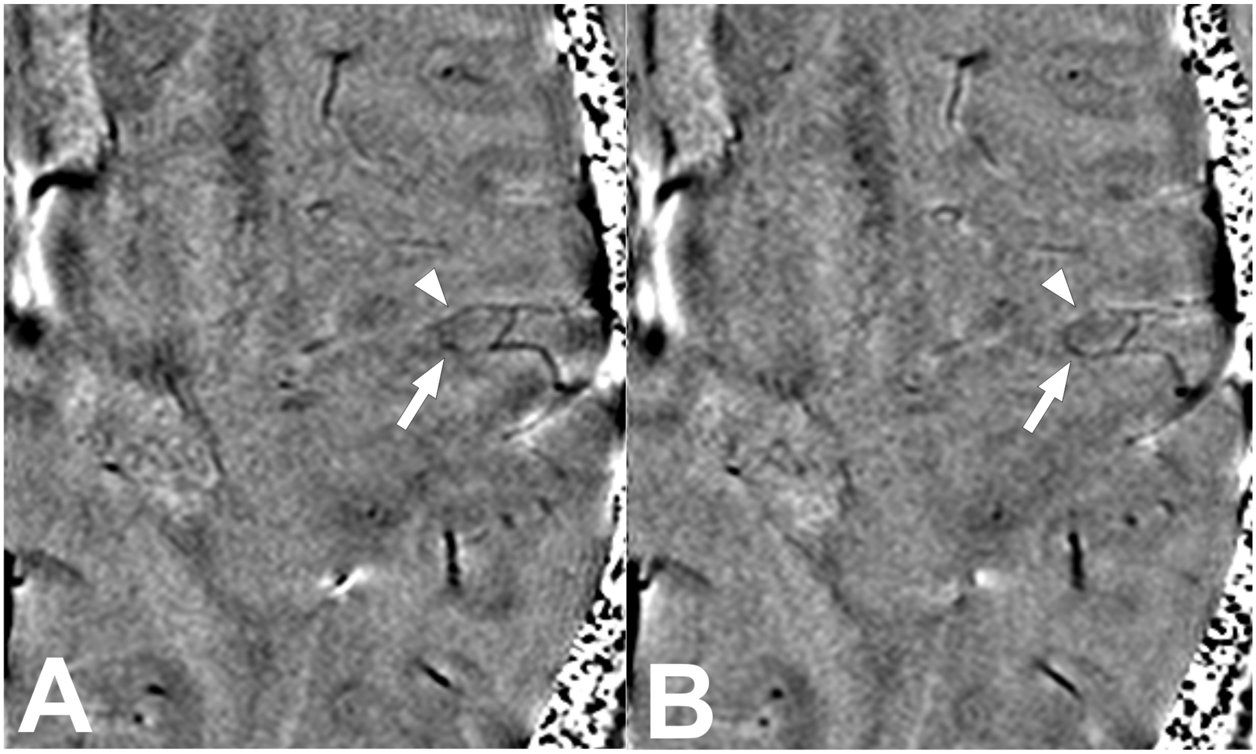

Figure 2.5. Downsampled phase images comparing A) k-space crop and B) complex averaging. Note the small vein (arrow) is better depicted in the complex averaging due to better partial voluming. The veins that the k-space crop shows slightly better (arrow heads) are equally well depicted in the complex filtering in adjacent slices (not shown). Images acquired at 3T with TE/TR/FA/BW = 20 ms/30 ms/15°/160 Hz/pixel.

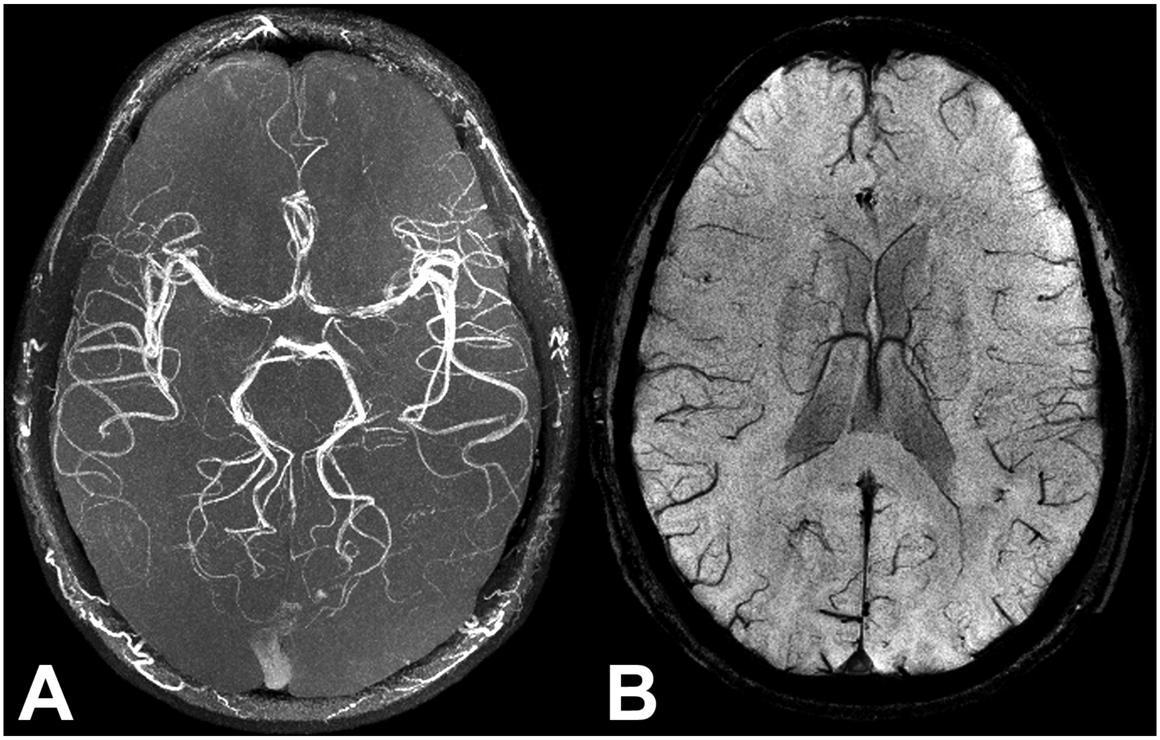

Figure 2.6. Single echo SWI dataset acquired at 3T with TE = 20ms, TR = 35ms, FA = 15°, BW = 160 Hz/pixel A) MIP over 64mm shows contrast comparable to a traditional MRA distal to the MCA which still has some flow related losses B) mIP over 8mm shows contrast comparable to a traditional SWI.

Combining all these techniques it is possible to acquire a single echo SWI scan that has both artery and vein contrast. The SWI contrast and venography, as shown in Figure 2.6, are of good quality with the veins being well depicted. Likewise, nearly all of the arteries are well depicted; however, there is some signal loss in parts of the fast-flowing MCA and carotid due to flow dephasing from the field inhomogeneities in that region. The more distal arteries are well depicted with little to no signal loss.

Conclusions and Future Directions

Blood properties at different field strengths

For brain parenchyma, the T1 values have been found to generally increase with field strength (Bottomley et al. 1984) and the T2 values do not change much until you get above 3.0T and then they start to fall precipitously (Jezzard et al. 1996). The T2* values of all tissues behave differently than the T2 values. They also fall with field strength but they begin to decrease at lower fields and change significantly between 1.5T and 3.0T (Peters et al. 2007). Relaxation values for blood are difficult to measure accurately as blood is constantly flowing and ex-vivo measurements can be challenging due to changes in oxygen saturation which can affect the results. However, T2* values for venous blood do decrease dramatically across commonly used field strengths and range from 97ms at 1.5T to 25ms at 3.0T and 7.4ms at 7.0T (Koopmans et al. 2008).

The decreasing values of T2* for all tissues as field strength increases has important implications for SWI. At 1.5T relatively long echo times (40 ms) are demanded to give time for significant T2* contrast to develop. These long echo times are also needed to develop adequate contrast in the phase image according to equation 1.2. But as field strength increases, the echo times can be shortened, approximately linearly with the increase in field strength, while still maintaining both T2* contrast and susceptibility contrast in the phase image. Phase contrast is maintained as equation 1.2 shows since it is dependent on the product of echo time and field strength, and T2* contrast from the veins in the magnitude image is maintained due to the falling T2* values with field strength. The reduced echo time allows a significant time savings in SWI as one moves to higher field strengths and also allows better flow compensation for better contrast in the large arteries. The shorter echo times available for SWI at high field strength make this single echo multi-contrast technique more viable as better MRA contrast can be achieved without sacrificing SWI contrast.

Role of T1 and T2 reducing contrast agents*

T1 shortening contrast agents, such as gadolinium traditionally used for MRA, can also substantially improve the quality of SWI venography. The T1 shortening of the contrast agent causes an increase in the available signal for blood. The deoxyhemoglobin in the blood causes a slight frequency shift in the venous blood (this is what causes the phase contrast); this frequency shift allows the echo time to be chosen such that venous blood and brain parenchyma are out of phase and the signals will cancel. This cancelation allows the shortened T1 and increased signal of the blood to improve contrast in the veins; this is referred to as T1-T2* coupling. The usual gadolinium based contrast agents are paramagnetic and for a 1mM concentration in the blood they increase the local susceptibility of the blood by 2/9ths of the usual BOLD effect. This in turn introduces an increase in the phase of the blood by 2/9ths, further improving SWI contrast.

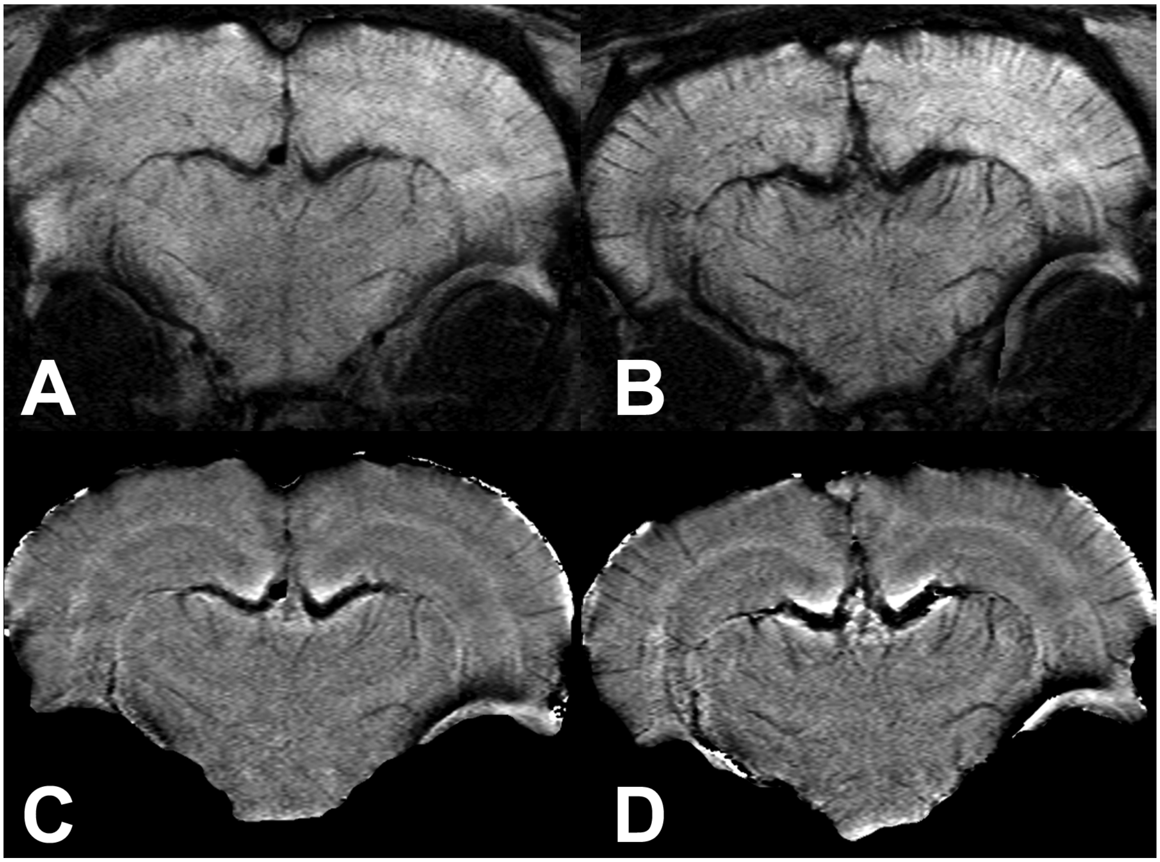

Figure 2.7. SWI of a rat anesthetized with isoflurane and oxygen. Left images show pre-contrast and right images are 2.5 hours post USPIO (P904, 300 µMol Fe/kg). Single slice SWI (top) and filtered phase images (bottom), notice the veins are much better visualized even 2.5 hours post contrast (image courtesy of Yimin Shen).

The possibility of using direct T2* shortening agents in the blood also exists with ultrasmall superparamagnetic iron oxides (USPIO) or superparamagnetic iron oxides (SPIO). While these have very large T2* shortening properties they act evenly on both arteries and veins which causes the arteries to go dark along with the veins. While this does cause artery/vein ambiguity, the level of small vessel detail seen is quite impressive (Figure 2.7). If this could be run in some sort of pre-post fashion to separate the arteries from veins it could find a use in imaging the small arteries of the brain as well.

The single echo method presented here is capable of producing SWI and MRA contrast comparable to traditional SWI scans and MRA scans with the exception of the MCA and carotid arteries due to some residual flow losses (Figure 2.6). The single echo method is still inferior to the double echo techniques in imaging larger arteries. However, it also has some advantages over the double echo techniques. First, both the arteries and the veins are visible on the same set of images. This could prove advantageous if one is interested in examining both the arterial and venous components of a tumor or an arteriovenous malformation (AVM) and how they relate to each other. Second, since both arteries and veins are visible on a single image there is no possibility of misregistration. While there is no chance for movement induced misregistration in the double echo sequence, eddy currents and different bandwidths used for the first and second echo can cause small shifts in the image and different distortion effects leading to a small amount of misregistration between the echoes. Fourth, if the single echo method were combined with a susceptibility mapping technique (de Rochefort et al. 2010), a shorter echo time could be used and still give adequate susceptibility contrast. These two techniques could complement each other nicely as the high resolution isotropic data that is collected for the single echo MRAV would be ideal for the susceptibility mapping algorithms. Finally, at higher field strength the optimal echo for SWI is much shorter which makes it more difficult to fit two echoes in this shortened time frame and improves the flow compensation for the single echo approach. This method could therefore find more use in high field (>3.0T) applications.

Future work in this area at 3.0T and below will probably focus on general multi-echo sequences (more than two echoes) as these can provide a variety of different contrasts and be used to generate accurate T2* maps. For high field studies (7.0T and above), including high field animal imaging, the single echo approach will give the best results. For example, at 11.7T an echo time of only 7 ms is required for good SWI contrast which makes a double echo sequence both more challenging and unnecessary.

CHAPTER 3 – HIGH RESOLUTION MRA

Introduction

The high resolution isotropic scans (0.5 mm in all directions) used in the previous chapter showed very good small artery contrast comparable with the best standard MRA sequences. It was hypothesized that these high resolution fully flow compensated sequences with a symmetric acquisition could achieve the necessary contrast to noise ratio to visualize arteries of approximately 100µm in diameter. In this chapter we sought to examine the sources of small vessel contrast and optimize acquisition parameters to maximize this contrast. Imaging these small arteries could be of interest to many diseases including being able to image the arteries responsible for the cerebral microbleeds (CMB) that are examined in the next chapter.

Current MRA techniques cannot image very small features of the vasculature. These small arteries are important for the understanding and diagnosis of diseases such as cerebral amyloid angiopathy (CAA) where the vessel wall becomes stiff and may bleed, detecting small aneurysms, detecting small arterial CMB caused by aging, Alzheimer’s and other pathologies (Greenberg et al. 2009), and measuring vessel tortuosity as a marker for cancer (Bullitt et al. 2007). This was the topic of my Master’s thesis, where resolution, MT pulse, contrast agents, and acquisition order were examined in detail (Barnes 2008). Here, a number of new ideas are proposed to further investigate this topic.

Multiple parameters were examined to determine their effect on small vessel contrast. The benefits were weighed against the cost (usually scan time) to determine if they were beneficial or if simply using averaging and scanning longer for better SNR was superior. The parameters examined were echo time, flip angle, and subtraction of pre-post contrast images. Finally, signal, contrast and noise levels were examined to predict visibility for a small 125 µm vessel on a modern 3T system with a 24 channel head coil at different resolutions.

Image Acquisition

Healthy normal volunteers were scanned at 3T with a 24 channel head coil using a fully flow compensated gradient echo acquisition. A variety of imaging parameters (as detailed below) were used as many different parameters were examined. Informed consent was obtained in all cases and the study was approved by the local ethics review board.

Results and Discussion

TE Analysis

Traditional MRA scans are run with as short a TE as possible, typically <5ms. To achieve this short of echo time an asymmetric echo is used. This very short echo time is used to reduce the higher order flow effects (such as accelerating blood) that are not compensated for, but it also has the advantage of reducing scan times as the TR can then be shortened. The high arterial contrast on SWI images and the single echo MRAV scans described in Chapter 2 suggested that the T2* value of arterial blood might be longer than that of the parenchyma leading to increased contrast at longer echo times. This approach would be most beneficial in small distal arteries that do not suffer from accelerating or turbulent flow and are distant from gross field inhomogeneities and therefore would not suffer flow related losses at longer echo times (see Chapter 2).

To determine the benefits of longer versus shorter echo time two volunteers were scanned with identical parameters at a TE of 11.3 ms and 20 ms, TR=30 ms, BW=120 Hz/pixel, FA=15°, and Resolution 0.5x0.5x0.5 mm^3. Since the small vessels are of interest a symmetric echo was used as an asymmetric echo will cause blurring and loss of contrast in small structures. The symmetric echo resulted in 11.3 ms being the minimum echo time possible. Contrast to noise ratio (CNR) measurements on the smaller arteries (that we are interested in) proved difficult as partial volumeing, has a large effect on vessel intensity. The measurements were therefore quite variable, but showed approximately a 0-10% increase in CNR at the longer echo time versus the shorter. To try and remove the variability from partial volumeing measurements on the MIPs were performed. This tended to be more reliable as it was possible to measure a larger section of vessel and it is a realistic assessment of the scan contrast as MRAs are commonly viewed as MIPs. The MIPs showed an increase in CNR of 5% in the long echo scan versus the short echo scan. This small increase in CNR did not correspond to any obvious visible change in vessel conspicuity and no new vessels were visible.

The minor increase in CNR (5%) at a longer TE does not justify the ≈50% increase in scan time. This 50% extra time could instead be used for signal averaging which would reduce the noise and increase the CNR by 22%. It is therefore not advantageous to acquire longer echo times to improve small artery contrast.

It is interesting to note that this increased contrast at longer echoes implies a relatively long T2* value for arterial blood, at least longer than the parenchyma which is 53-66 ms (Peters et al. 2007) at 3T. Unfortunately, there are no literature values for the T2* of oxygenated blood at 3T and it is very challenging to measure in vivo due to the rapid flow in large arteries and the partial voluming in small arteries with slower flow. In vitro scans are also challenging as the oxygenation must be maintained at physiologic levels due to the strong paramagnetic effects of deoxygenated hemoglobin which alter the T2* values.

We made three attempts to quantify the T2* of arterial blood. Two different volunteers were scanned using a double echo sequence run twice to get a total of four echoes. The parameters used were TR=45 ms, FA=25°, BW=360/255 and 310/310 Hz/pixel, and TE=7.4/21.5, 15/38.9 and TE=7.4/29, 18/39 ms. The third volunteer was scanned with a single echo sequence run three times for a total of three echoes with parameters TR=28 ms, FA=15°, BW=120 Hz/pixel, and TE=11.3/15/20 ms. The T2* values measured had a very large variance with the values ranging from 40 ms to 100 ms depending on the artery selected and the acquisition analyzed. The large variance is most likely due to uncompensated flow effects decreasing the apparent T2* value. This effect would be inconsistent across different arteries, and could explain most of the variance seen. It would also be more problematic in the larger arteries, which were the ones analyzed due to the difficulty in reliably defining an ROI across multiple scans in the small arteries. However, partial volumeing and patient motion between scans could also be contributing factors. The contrast measurements suggest that the true T2*, discounting flow effects, is closer to the 100 ms end of the range due to the increasing contrast in small vessels at longer echo times.

Figure 3.1. MIP over 8mm (16 slices) TE = 11.3ms on left, and MIP over 8mm (16 slices) TE = 20ms on right. Notice the parenchyma is slightly darker at the longer echo time leading to a very slight increase in small artery CNR.

FA Analysis

The optimal FA to run depends on the effective T1 of the arterial blood and parenchyma and the TR of the scan. This should be a straight forward calculation maximizing the difference in signal intensity between the parenchyma and arterial blood using the FLASH equation

$$Contrast_{a-p} = \frac{\rho_a \cdot \sin(\theta) \cdot (1-e^{-TR/T1a})}{1-e^{-TR/T1a} \cdot \cos(\theta)} - \frac{\rho_p \cdot \sin(\theta) \cdot (1-e^{-TR/T1p})}{1-e^{-TR/T1p} \cdot \cos(\theta)} \quad (3.1)$$

where T1a, T1p, ρ_a, and ρ_p, are the T1 and spin densities values of the arteries and parenchyma respectively. However, the effective T1 of the arterial blood changes based on inflow (hence flow rate, slab thickness, and position within the slab) and contrast agent concentration (if used). These considerations can cause the effective T1 of blood to change by an order or magnitude which means the FA choice must be optimized for a specific situation or a compromise for decent contrast in a wide range of situations.

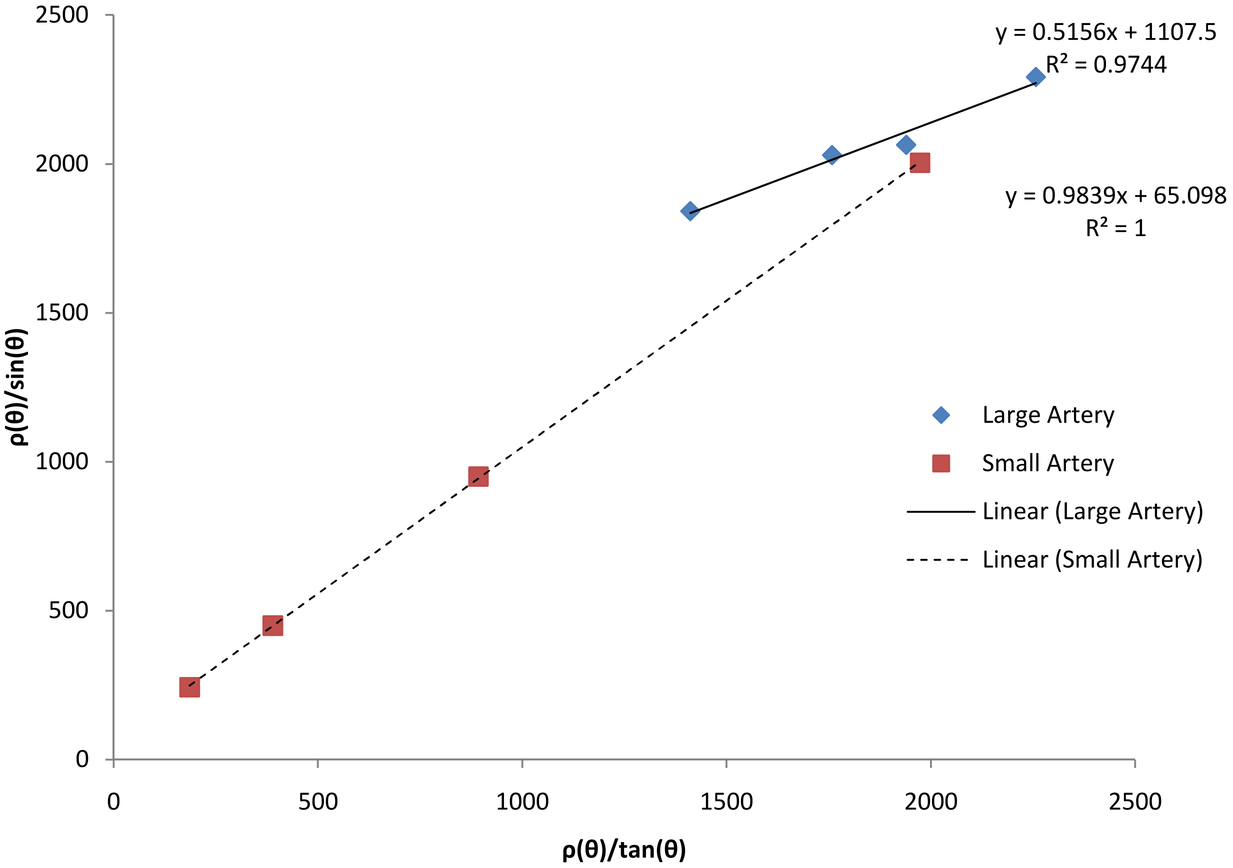

Figure 3.2. This graph shows the T1 measurements for both a large (with high inflow) and small artery (with little to no inflow). This shows that the effective T1 of the large artery is 48 ms due to fast inflow, where the small artery has an effective T1 of 1848 ms.

To obtain T1 values for this calculation, a measurement without a contrast agent was performed on a volunteer by running a series of four flip angles at 10, 20, 30, and 40 degrees with TR=30 ms, TE=11.3 ms, and BW=120 Hz/pixel. The T1 was then calculated by doing a linear regression fit to the signal intensity scaled by sin(θ) in the y direction and tan(θ) in the x direction (see Figure 3.2 for the arterial blood fits). A very good linear fit was obtained for all tissues and the T1 was calculated according to the formula

$$T1 = \frac{-TR}{\ln(m)} \tag{3.2}$$

where m is the sloop of the regression fit. An effective T1 of 45±8 ms and 1843±580 ms were calculated for the large and small arteries, respectively. The large artery was chosen was the M2 segment of the MCA, the small artery was an M4 segment. A value of 1845±149 ms and 1150±65 ms for gray matter and white matter were also calculated. The gray and white matter are in good agreement with literature values of 1820±114 ms and 1084±45 ms, respectively, and the small artery value is close to that of venous blood, 1932±85 (Stanisz et al. 2005).

These T1 values indicate that the small arteries do not have significant inflow as there T1 value is nearly identical to the literature reported T1 value of venous blood. The small artery analyzed was located only 15 mm into the slab, so using thinner slabs to increase inflow probably isn’t practical. Therefore, to image the small arteries it is necessary to use a contrast agent as there is very little enhancement from inflow. The choice of FA must then be based on contrast agent concentration which will be the dominant effect on the T1 values in small arteries.

It is also interesting to note that the large difference in the intercept of the two lines in Figure 3.2 is due to a difference in effective T2* between the fast flowing larger artery and slow flowing small artery. The intercept corresponds to

$$\rho_0 e^{-TE/T2^*}(1 - e^{-TR/T1}) \tag{3.3}$$

where ρ_0 is the spin density of arterial blood. Removing the above T1 term from the calculated intercepts (1108 and 65 in Figure 3.2) using the estimated T1 value from the slope gives values of 2286 and 4043 for the large and small arteries, respectively. These values depend on just the ρ_0 and T2* terms in equation 3.3. If we assume the spin densities are the same this means that the T2* term causes the signal to decay by almost a factor of two in the larger artery compared to the small artery at the echo time of 11.3 ms. This lends further weight to the previous argument that different flow effects will cause a large variance in the measured T2* values of arterial blood despite the use of flow compensation.

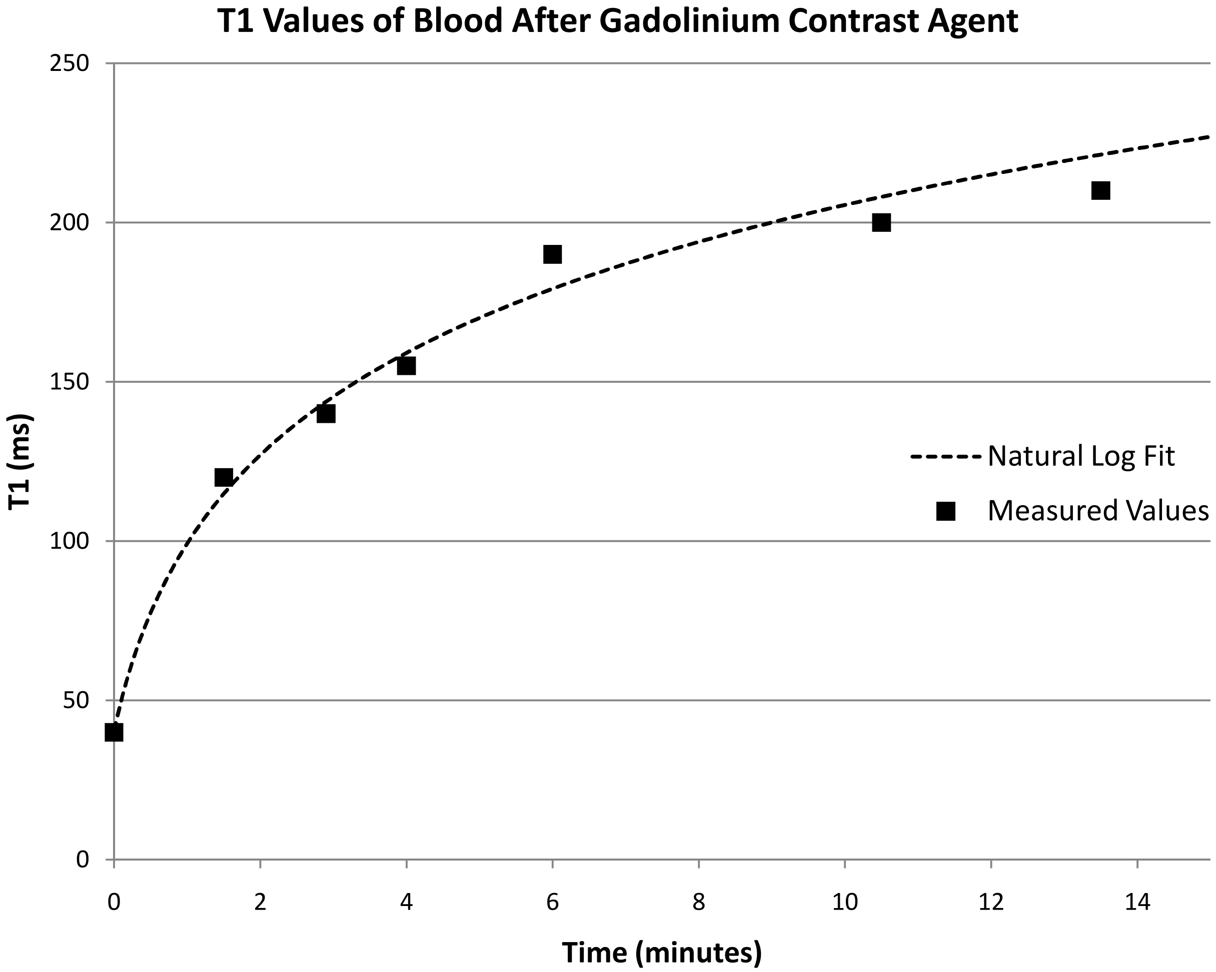

Figure 3.3. T1 values versus time measured after contrast agent injection as presented by Bosmans (Bosmans et al. 1995), the dashed line is a natural log fit to those values. The first point in the curve is an estimated value for the first pass of the bolus.

The T1 values of arterial blood after contrast agent injection taken as reported in the literature (Bosmans et al. 1995) can be seen in Figure 3.3. For a long 10-15 minute scan the T1 value of blood varies significantly as the contrast agent starts to be filtered out by the kidneys. Still for most of the scan the T1 value will lie between 100 and 200 ms. If we take this as the range of values that we want to optimize for we can easily use equation 3.1 to calculate that a good choice of FA is 30°. This is slightly below the optimal FA for a T1 of 100 ms and slightly above the optimal FA for a T1 of 200 ms (see Figure 3.4).

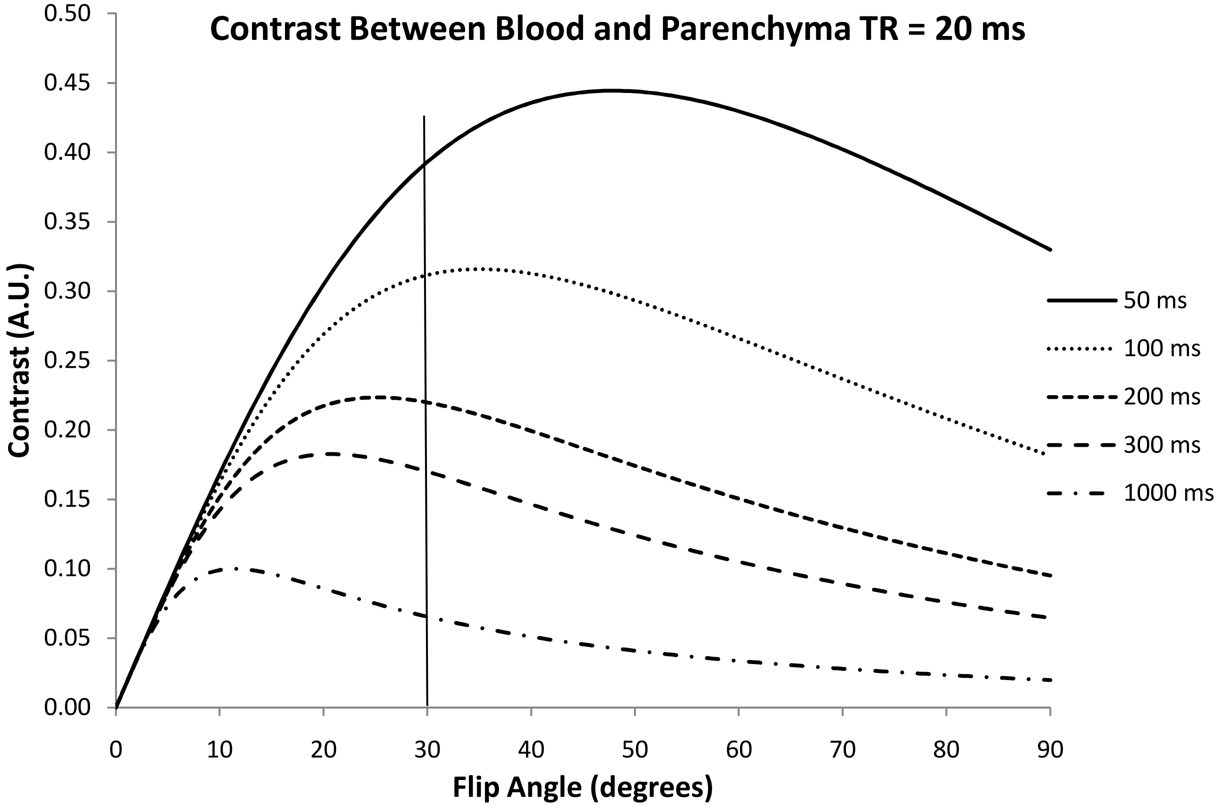

Figure 3.4. This graph shows the optimal contrast between parenchyma (T1=1800 ms) and blood for different T1 values of blood. Selecting a flip angle of 30° is near optimal for a wide range of blood T1 values, from 300 ms to 100 ms. A value of 30° only gives suboptimal contrast for T1=50 ms which should only occur in the first minute or <10% of the scan time (Figure 3.3) or in the very large vessels (from inflow, see above) which are well visualized anyway.

Figure 3.4 also shows the potential to increase contrast in the small vessels if a larger dose of contrast agent or a contrast agent with a higher relaxivity were used. The use of a contrast agent that would decrease the T1 in small vessels from 200 ms to 50 ms could increase the contrast in the vessels by a factor of 2.4.

Subtraction Analysis

Background suppression can be improved by subtracting pre/post contrast images. Since the very small arteries have almost no enhancement pre contrast their signal is not reduced very much while the background tissue should subtract out almost completely. This technique does increase the noise by a factor of $\sqrt{2}$ and suffers from misregistration if the subject moves between scans which can be particularly problematic with high resolution long scans. This can be partially corrected with the use of registration algorithms, but these inevitably blur the image, reducing quality. An example subtracted dataset is shown in Figure 3.5. In this nearly ideal case with virtually no motion between scans you can see that the background is significantly reduced increasing small vessel contrast. The increased noise is also apparent in the vessels.

This example case was collected with parameters TR=20 ms, TE=11.3 ms, FA=30°, BW=120 Hz/pixel, and a resolution of 0.5x0.5x0.5 mm^3. While subtraction does increase vessel conspicuity in the example case we collected it did not reveal additional vessels. The increased noise, very long scan times (double a normal scan as it must be run twice), and problems with subject motion do not make this a practical solution. There are also limits to how much background suppression can increase the contrast in small vessels as the background signal cannot be decreased below the noise level. Even with perfect background suppression the predicted CNR for a 125µm vessel is below the visible level for current resolutions and signal-to-noise ratios (see Table 3.1).

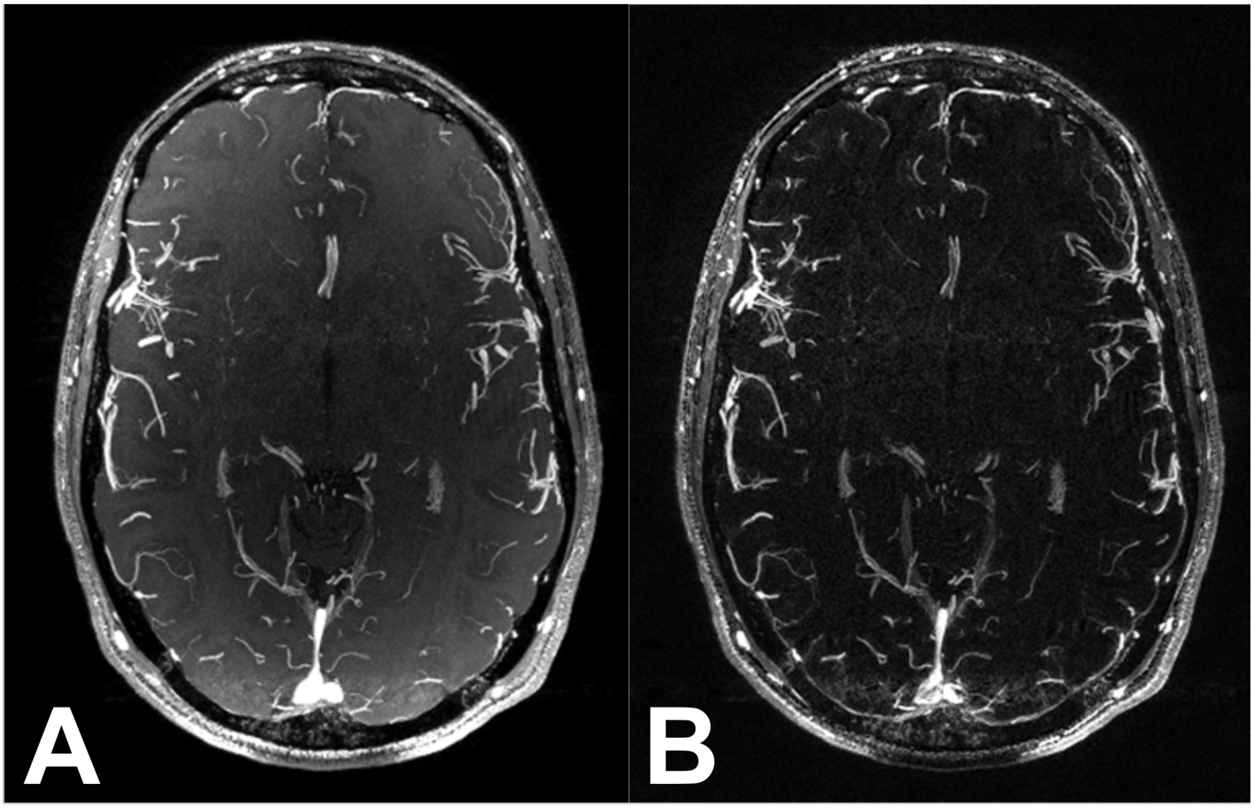

Figure 3.5. MIP over 4mm, from a scan with a resolution of 0.5x0.5x0.5. Left post contrast, right subtraction of pre and post contrast.

Resolution Analysis

The signal intensities of the arteries, parenchyma, and noise levels were all measured in a post gadolinium scan with a resolution of 0.5x0.5x0.5 mm^3. These values were then analyzed and used to predict the CNR for a 125 μm vessel at various resolutions and with a hypothetical prefect background suppression technique (Table 3.1) representing an idealized best case scenario. The vessel is assumed to run perpendicular to the imaging slice so slice thickness was not considered.

If we make the standard assumption that an object will only be visible with a CNR of 4 we see that even with perfect background suppression, a 125 μm vessel will not be visible on a 500 μm scan at current noise levels, and would barely be visible with a 250 μm scan. This means that for a more realistic model of background suppression, the resolution needs to be comparable to the size of the object to detect it. Even when a contrast agent is used, nearly 125 µm resolution is needed to see 125 µm objects for current signal levels.

To image small vessels, further gains must be made with either noise reduction (averaging, more coils, higher field, cryogenically cooled coils), increased resolution (to 125 x 125 µm^2), or increased signal from blood (higher concentration of contrast agent, higher relaxivity contrast agent). Improving background suppression will add very little to the visibility of small vessels.

Voxel Size x,y (µm)		Relative time	GM	Blood	Noise	125µm Vessel	Contrast	CNR	125µm Vessel	Contrast	CNR
500	500	1	173.0	475.0	12.0	*187.8*	*14.8*	*1.2*	*23.3*	*23.3*	*1.9*
250	*500*	*1*	*86.5*	*237.5*	*8.5*	*101.3*	*14.8*	*1.7*	*23.3*	*23.3*	*2.7*
250	*250*	*2*	*43.3*	*118.8*	*6.0*	*58.1*	*14.8*	*2.5*	*23.3*	*23.3*	*3.9*
125	*250*	*2*	*21.6*	*59.4*	*4.2*	*36.4*	*14.8*	*3.5*	*23.3*	*23.3*	*5.5*
125	*125*	*4*	*10.8*	*29.7*	*3.0*	*25.6*	*14.8*	*4.9*	*23.3*	*23.3*	*7.8*

🟨 = Values for typical intensity of background
🟩 = Values if we had perfect background suppression
Italics = Predicted Values

Table 3.1. Measured and predicted signal, noise, contrast and CNR values for a 125 µm diameter vessel. A CNR value of 4 is considered necessary for an object to be visible.

The observed intensities of larger vessels, which exhibit much shorter effective T1 due to inflow, give hope that increasing the signal from the small blood vessels is feasible. As mentioned above, if a strong contrast agent could be used to achieve a T1 of 50 ms in small vessels (making their effective T1 equivalent to that of large vessels) it could make a 125 µm vessel visible on a 500 x 250 µm^2 scan (predicted CNR 4.1) and definitely on a 250 x 250 µm^2

scan (predicted CNR 6.0) which is an achievable resolution using current techniques (Barnes 2008).

To reduce the noise you could increase the number of averages (N_{acq}=2) as a proof of concept. The current protocol is only 8 minutes long so running two acquisitions would only be 16 minutes which might be possible with a good volunteer. This would reduce the noise by a factor of $\sqrt{2}$. This would increase the CNR enough to make vessels visible on the 250 x 125 μm^2 scan (predicted CNR 5.0). However, since the resolution in the phase encode direction has doubled the scan time would double to 32 minutes. Practically this is not feasible (due to inevitable subject motion) so noise reduction would have to be sought in other ways, either improved coil design or higher field. Finally, these calculations also show that based on the intensities of the vessels we can see, we are not able to visualize any arteries smaller than 250 μm.

Conclusions and Future Directions

To image the very small arteries of the brain this work has shown the necessity of using high relaxivity contrast agents (due to poor inflow) and also the importance of scanning at very high resolution. Our findings indicate that T2* of venous blood decreases much faster than T2* of arterial blood even at 3T. This provides an opportunity to clearly separate arteries and veins using MRA and SWI, respectively.

While we see tantalizing hints of the next level of arteries in these scan (Figure 3.6), we have shown that the bulk of these small arteries (which are thought to be on the order of 100 μm (Barnes 2008)) will not be visible without substantial improvements in CNR achieved through either: higher relaxivity contrast agents, improved coil design, higher field strength, or a radically different acquisition technique.

Some recent work has shown that the new contrast agents that are being developed with much higher relaxivities could indeed allow the imaging of 100 μm vessels at current clinical field strengths (1.5 – 3.0T) (Lee et al. 2009). Unfortunately these agents are not currently approved for human studies and probably will not be in the near future so no human studies are possible at this time.

Human studies at higher field strengths (7.0T), on the other hand, are already allowed. The near doubling of SNR compared to 3.0T should allow these vessels to been seen at the very achievable resolution of 250 μm. The lack of approved high relaxivity contrast agents for human studies suggests that future human studies in this area will be carried out at high field with traditional contrast agents.

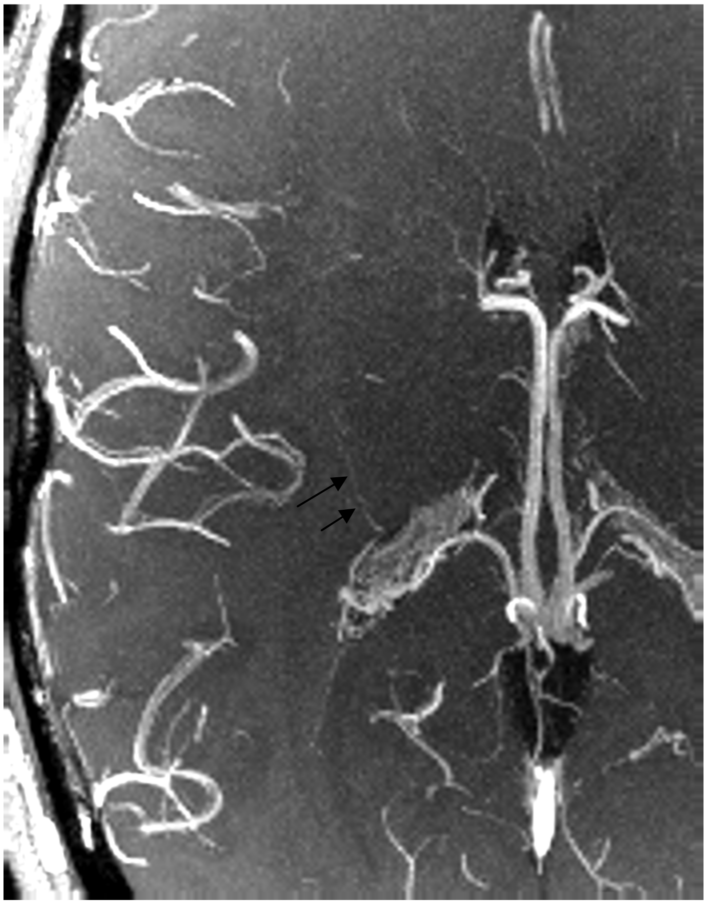

Figure 3.6. Arrows indicate possible 250μ vessel based on intensity measurements. MIP over 16 slices (8mm).

CHAPTER 4 – SEMI-AUTOMATED DETECTION OF CEREBRAL MICROBLEEDS IN MAGNETIC RESONANCE IMAGES

Introduction

Cerebral microbleeds (CMB) are generally defined as asymptomatic small bleeds (diameter <5-10 mm) seen primarily with a magnetic resonance imaging (MRI) T2*-weighted scan (Greenberg et al. 2009). It has been shown that MR-visible CMBs consist mostly of hemosiderin (Fazekas et al. 1999; Schrag et al. 2009), whose large susceptibility effect accounts for good visibility in T2*-weighted scans. Individuals with cerebrovascular disease related dementia and even a subset of the healthy aged population develop CMBs. While CMBs are usually asymptomatic, they can be important clinical indicators of different diseases. The presence of CMBs can suggest an increased chance of lacunar infarction, intracerebral hemorrhage, or hemorrhagic stroke in patients already suffering from these pathologies (Fan et al. 2003; Greenberg et al. 2004; Imaizumi et al. 2004). Increasing numbers of CMBs indicate a worsening of dementia upon follow-up after primary lobar intracerebral hemorrhage (Greenberg et al. 2004). In another longitudinal study, a temporal increase in the number of CMBs was correlated with worsening dementia (Ayaz et al. 2009). CMB detection is becoming an important tool for non-invasive detection of diseases like cerebral amyloid angiopathy (CAA), CADASIL (cerebral autosomal dominant arteriopathy with subcortical infarcts and leukoencephalopathy) and hypertension (Greenberg et al. 2009). For more details on CMBs please refer to these excellent reviews (Cordonnier et al. 2007; Greenberg et al. 2009).

CMB contrast and detection is sensitive to many imaging variables such as field strength, echo time and resolution (Greenberg et al. 2009; Nandigam et al. 2009). Modern imaging protocols such as susceptibility weighted imaging (SWI), that are routinely run at high resolution (≤1mm^3), long echo time, and use the phase image to enhance contrast, are much more sensitive in detecting small bleeds than traditional protocols (Ayaz et al. 2009). Recent publications have shown that when SWI is compared with standard gradient echo imaging there is a three to six-fold increase in the number of CMBs seen (Tong et al. 2003; Nandigam et al. 2009).

CMBs are, by definition, small and are easy to confuse with other structures (so-called CMB mimics (Greenberg et al. 2009)). The small size and large numbers of CMBs and CMB mimics have hampered efforts to quantify their number and volumes. So far, methods have centered on manually identifying and drawing the lesions, or manually defining local thresholds for a small region of interest (ROI) (Ayaz et al. 2009; Greenberg et al. 2009). These methods suffer from a high amount of inter- and intra-observer error (Cordonnier et al. 2009) and become extremely time-consuming as the number of patients and CMBs grows. In manual identification, a set of rules can be defined to determine whether any small hypointensity is a CMB (Ayaz et al. 2009) to help improve consistency. Recent publications have shown improvements by using standardized rating scales (Cordonnier et al. 2009) but further improvement in consistency, speed of identification and quantification are desirable.

Automatically identifying the CMB is problematic as there are many dark structures on SWI images that can easily be confused with CMBs. Most notably, SWI's excellent venous contrast makes veins also appear dark. Any method that seeks to identify CMBs will need a way to differentiate CMBs from venous structures. We propose that after marking all dark structures, characteristic features (notably shape) can be calculated and used to separate CMBs from veins with the use of a support vector machine (SVM) classifier.

In this work we propose a semi-automated method of identifying and quantifying CMBs seen on high resolution SWI scans. This method has four steps: 1) a pre-processing step that consists of image interpolation and brain extraction to remove the skull and background, 2) statistical thresholding that marks all hypointensities, 3) an SVM classifier that eliminates hypointense noise and veins, and finally, 4) a manual review of results to eliminate the remaining false positives (Figure 4.1). The manual intervention is limited to making yes or no decisions on the automated suggestions which reduces processing time and observer variability.

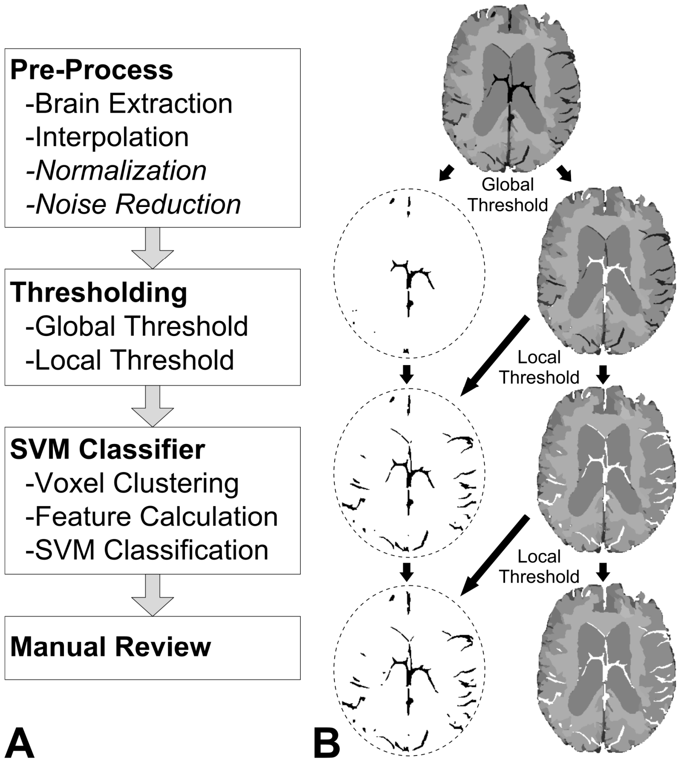

Figure 4.1. A) Flowchart of processing steps, the two pre-processing steps in italics were not used in these datasets but might be useful for other types of data. B) Schematic showing thresholding step in more detail. Each thresholding iteration marks additional voxels that are added to the final results and excluded from the next iteration.

Materials and Methods

Data Collection

All SWI images were acquired as part of a longitudinal study on individuals with mild cognitive impairment or early Alzheimer's disease (Kirsch et al. 2009). Data were collected at 1.5T using a fully flow compensated 3D gradient recalled echo (GRE) sequence with a resolution of 0.5x1.0x2.0 mm^3 and a matrix of 512x320x48. Imaging parameters were: TR=57ms, TE=40ms, FA=20°. Standard SWI processing with high pass filtered phase images was performed (Haacke et al. 2004). A total of six datasets (containing 126 CMBs) were processed with this method.

A manual review of the data was performed independently by three reviewers using a standard set of criteria (Ayaz et al. 2009). All three reviewers then compared results and reached consensus when differences in counts were encountered. All results were reviewed by a senior neuroradiologist (DK). More details on the manual review can be found in (Ayaz et al. 2009).

Pre-Processing: Brain Extraction and Interpolation

Brain extraction was accomplished with a thresholding technique based on the magnitude and phase data. Regions of no signal were identified as those having low intensities in the magnitude image and uniform noise distribution over all values in the phase image. By using both the magnitude and phase, the accuracy of the extraction is improved compared to using either independently (Pandian et al. 2008). Isolated islands of points (<5000 voxels) were removed and isolated holes (<1000 voxels) in large regions were restored to their original values to remove remnant skull and restore any holes inside the brain, respectively. Finally, an erosion of three voxels was performed to remove partial-volume brain tissue that has a lower intensity and hence creates a rim artifact that is picked up in the thresholding step.

After the brain extraction, the images were interpolated by two in the X and Y directions. This interpolation allowed for better shape definition of small structures and leads to better classification. A given marked structure of three uninterpolated voxels can assume only two different shapes (a line and an ‘L’ shape), making it hard to get meaningful shape information. Upon interpolation, this same structure will be 12 interpolated voxels, which can form a wide variety of shapes—making shape a more robust identifying feature.

Local Statistical Thresholding

Local statistical thresholding is used to separate the Gaussian distribution of background tissue from the low outlier CMBs. Our implementation of local statistical thresholding calculates the threshold based on the mean and standard deviation of the surrounding tissue. We assume a white noise distribution in the parenchyma for a roughly Gaussian distribution with a small number of low-intensity outliers (potential microbleeds, vessels, other objects of low signal intensity) that do not significantly alter the mean or standard deviation of the region. To identify the CMBs, we seek to model the Gaussian distribution by calculating the mean and standard deviation, then setting a threshold to be a certain number of standard deviations below the mean to separate the parenchyma from the outliers. This method will fail if the number of low outliers is too large, making the distribution non-Gaussian, lowering the mean and increasing the standard deviation. To help prevent this, two restrictions are placed on the mean and standard deviation calculations. First, before local thresholds are calculated, an initial whole-brain global threshold is performed to identify and exclude large dark structures that would skew the calculation. Second, the local thresholding is iterated with previously marked voxels from the global and local thresholds being excluded from subsequent calculations to improve the accuracy of the calculated mean and standard deviation.

The global threshold intensity is preset to a conservative value where only very dark structures (usually the large ones) are marked (Figure 4.1b and 4.2a). This step aims to remove large structures, such as large veins, that could skew the mean and standard deviation values that are calculated in the local statistical thresholding. The voxels marked in the global threshold step are not used for the mean and standard deviation calculations in the next step but are marked as low outliers and included in the local thresholding results of potential CMBs.

Local thresholding is performed next (Figure 4.1b and 4.2b). A small ROI (size 40x40x5 voxels) centered on a single voxel is considered. In this ROI, the mean and standard deviation are calculated, excluding any points that have been previously marked. A local threshold is then calculated to be $\alpha \cdot \sigma$ below the mean, where σ is the standard deviation. If the voxel of interest is below this value, it is marked.

$$voxel_{marked} \quad < \bar{x}_{local} - \alpha \cdot \sigma_{local} \tag{4.1}$$

$$voxel_{background} \geq \bar{x}_{local} - \alpha \cdot \sigma_{local} \tag{4.2}$$

where α sets the degree of thresholding and can be adjusted for different types of data and different signal-to-noise ratios (SNRs). Generally, α = 2.5 gave good results for the datasets tested and was used to process all data. The area of interest is then moved and the process is repeated until a threshold has been calculated for every voxel and the entire image has been processed. In practice, calculating a new threshold for every single voxel proved too computationally expensive, so a single calculated threshold was applied to the center group of 5x5x3 voxels, rather than to the single center voxel. This provided a decrease in computation time by a factor of 75 with little effect on the end results.

This local thresholding process was then iterated. After the entire image has been processed, all thresholds are recalculated with previously marked voxels excluded from the mean and standard deviation calculations. Each successive mean and standard deviation calculation therefore includes fewer low outliers and a more accurate threshold is obtained. This improves the identification of edge voxels and small structures that might be located next to a large dark structure (a large vein for example). Practically, three iterations were run since little change was noted for higher numbers of iterations.

The size of the 40x40x5 region used to calculate the mean and standard deviation can also be adjusted to help ensure a Gaussian distribution. A smaller region gives more localized results but runs the risk of having its mean dominated by a large bleed or vein in the area. A larger region is less likely to be non-Gaussian but is also less sensitive to local information. A balance must be struck between the two and a relatively small area of 40x40x5 voxels was found to be a good compromise. The volume of the CMBs is significantly smaller than this so they do not significantly skew the distribution. In this way, the technique is optimized to detect small structures; larger structures will only be detected if they are dark enough to be picked up by the initial global threshold.

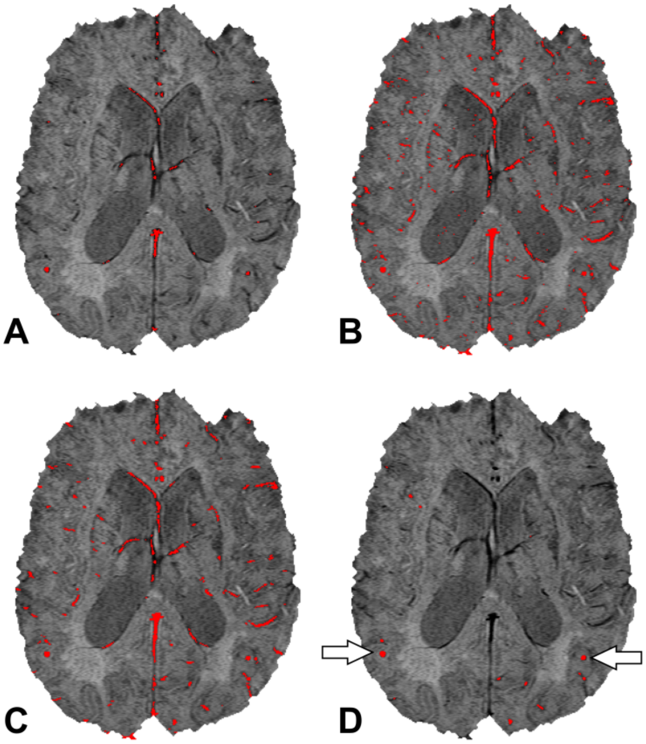

Figure 4.2. Shows the intermediate results after different thresholding steps on a single slice. A) Shows the results after the whole brain global threshold. B) Shows the results of the local statistical threshold before removing small clusters (assumed to be noise). C) Shows results of local statistical threshold after removal of small clusters. D) Shows the results of the SVM classifier which removes most false positives (veins and other dark structures).

Support Vector Machines

Support vector machines (SVMs) are a type machine learning supervised classifier. In our application they are used to do a binary classification between two classes of objects: CMBs and noise. For this type of binary classification, they seek to define a separating hyperplane between each class that both maximizes the distance between each class and the hyperplane (a maximum margin classifier) and minimizes the number of incorrectly classified objects. This makes the SVM a very general and robust type of classifier (Vapnik 1998).

SVMs take advantage of the so-called kernel trick to transform the original features into a higher dimensional Hilbert space. The maximum margin hyperplane is derived in this high dimensional space. The hyperplane is then transformed back from the high dimensional Hilbert space into the lower dimensional feature space. This is a nonlinear process that transforms the linear hyperplane into a nonlinear separation.

Classification – Feature Selection

Applying a classifier to the thresholding results is a necessary step to reduce the large number of false positives that are generated (see Table 4.1). The false positives are largely generated by dark veins, although some noise and susceptibility artifacts (such as those near the sinuses) also are marked. To remove these false positives a SVM classifier is used.

Before the classifier can be used, all marked voxels are sorted into connected clusters, where a cluster is defined as all marked voxels that are adjacent to one another. Each cluster is treated as a single object and is kept or discarded in its entirety. Clusters less than or equal to 10 interpolated voxels (equivalent to 2.5 voxels on the original datasets) are automatically removed as they are assumed to be noise (Figure 4.2b and 4.2c). Relevant features about each cluster (such as shape and intensity) are calculated and used by the classifier to make a “keep” or “discard” decision about each cluster (Figure 4.3). Feature selection focused on shape, size and intensity to distinguish CMBs from all other marked structures.

CMBs have a very characteristic shape—they are nearly spherical, making shape features the best identifying features. To this end, five different shape features were calculated and used: compactness, the three eigenvalues of the covariance matrix and the relative anisotropy (RA) calculated from these eigenvalues. These features were calculated as described below.

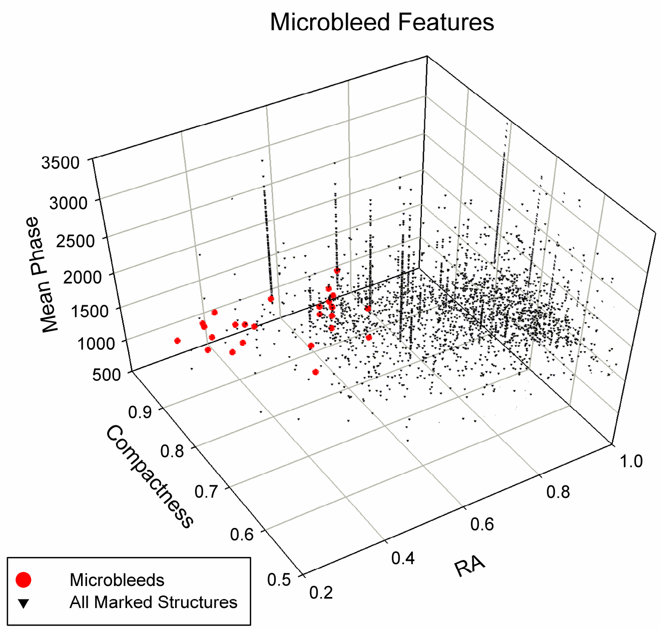

Figure 4.3. A plot of three features (out of the 14 used) that can be used to identify CMBs. The black triangles show all marked voxel clusters as generated by a statistical thresholding algorithm, the red circles are the clusters which correspond to actual CMBs as determined by manual inspection of the dataset. Using these features, it is possible to obtain a subset of a few hundred suspected CMBs which can be quickly sorted manually. The red circles are drawn larger to make them more visible.

Compactness is approximately a ratio of surface area to volume, with spheres having the highest theoretical compactness. CMBs therefore have a very high compactness and veins have a very low compactness. Since we are dealing with discrete voxels, compactness is calculated by counting adjacent voxel faces:

$$C_d = \frac{A_C - A_{C_{\min}}}{A_{C_{\max}} - A_{C_{\min}}} \tag{4.3}$$

where A_C is the actual number of adjacent faces, $A_{C\min}$ is the minimum number of adjacent faces possible for that particular number of voxels, and $A_{C\max}$ is the maximum number of adjacent faces possible for that particular number of voxels. More details can be found in (Bribiesca 2000).

The covariance matrix is a three by three matrix that describes mass distribution (Wasserman 2004). The eigenvalues and eigenvectors calculated from this matrix describe the principal axis. Thus, a spherical distribution would have three equal eigenvalues while a cylindrical distribution would have one large eigenvalue and two small eigenvalues. The eigenvalues were used individually as features and also combined to create an RA value using the standard formula

$$RA = \sqrt{1/2} \cdot \frac{\sqrt{(a-b)^2 + (b-c)^2 + (c-a)^2}}{a+b+c} \tag{4.4}$$

where *a*, *b*, and *c* are the eigenvalues of the covariance matrix of the cluster, *a* being the largest and *c* being the smallest. RA is a measure of how anisotropic a shape is, or how non-spherical it is, so CMBs should have a low RA value.

In addition to shape features, intensity and size were also used. A total of eight intensity features were calculated for each cluster: minimum, maximum, mean, and standard deviation for both the magnitude and phase images. The intensity features helped further characterize the CMBs and give the classifier more information to use. Finally, size was also included as a feature. While size alone is not a good criterion for identifying CMBs (Greenberg et al. 2009) other characteristic features (such as shape) might change with the size of the CMB. Having the size information thus allows the classifier to select the best set of identifying features for each different size of CMB.

Classification – Training

For the SVM we used the open source library libSVM version 2.88 (Chang and Lin 2001). This was chosen due to its wide use, good documentation, and open source availability so it could be easily integrated with our in-house C++ program (SPIN) in which all the other programming was implemented. A radial basis function was used, all features were scaled from 0 to 1, and the CMB class was weighted by a factor of 100. The radial basis function was chosen as it has been shown to give similar behavior as other commonly used basis functions (linear, and sigmoid) for certain values of model parameters cost and gamma and have less numerical difficulties compared with polynomial kernels (Hsu et al. 2003). Feature scaling was implemented to give all features equal weighting. If feature scaling is not used, the features with larger amplitude generally contribute more to the classification, possibly skewing the results. Finally, a weighting factor of 100 was used to offset the number disparity between the two classes. Approximately 15,000 true negatives and only 120 true positives were used to train the classifier so the most accurate naïve classification is to mark no CMBs, yielding an accuracy of over 99%. To correct for this, the CMB class was weighted in the classifier as more important to prevent this trivial case.

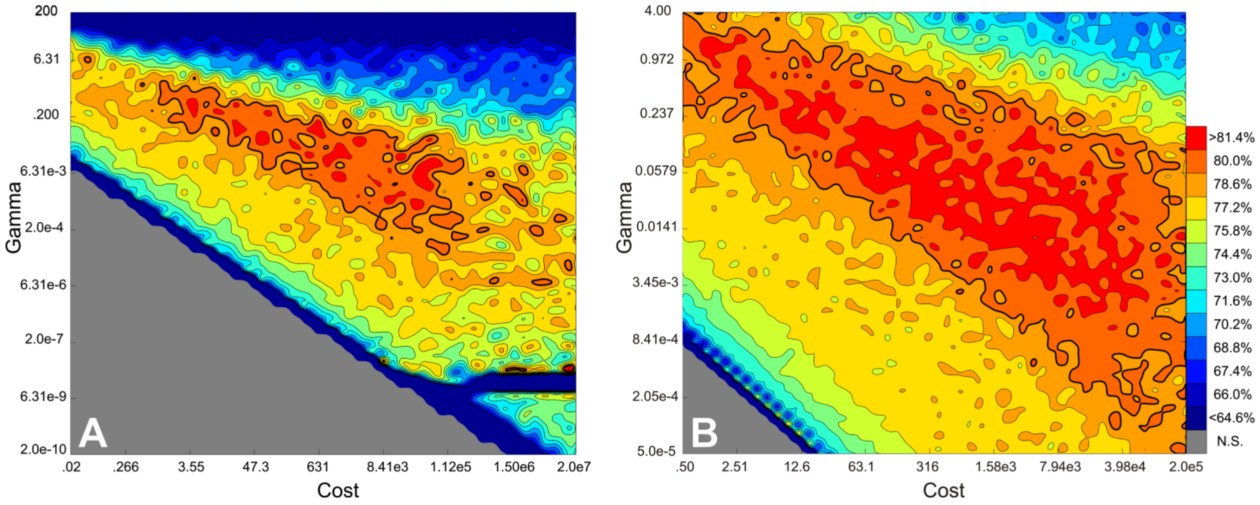

Figure 4.4. Parameter selection of cost and gamma using cross validation. a) A large parameter space was originally examined with nFold of 2 (half dataset used for training half for testing) to identify the best region for a more detailed examination. b) A more detailed examination of a smaller parameter space with nFold of 5 (4/5 of the dataset used for training 1/5 for testing repeated 5 times). The gray area represents parameters that weren't tested due to their consistently low values.

Training the SVM is an important step that can dramatically influence the accuracy of the classifier. Proper parameter selection, feature selection, class weighting, and feature scaling can all have a large influence. The cost and gamma model parameters control how the classifier behaves and must be selected based on the type of features one is using. To find optimal values a cross validation technique was used. In cross validation, the complete dataset for which the ground truth is known is randomly divided into testing and training portions, the classifier is trained on one portion and tested on another, and the accuracy of the test portion is then recorded. In this way, different values of cost and gamma can be examined and their accuracy determined. A course grid of cost and gamma values was first sampled to find the general area of best performance, a region of good performance was identified and that area was more tightly sampled (Figure 4.4). The cost and gamma values with the maximum accuracy from the tighter sampling were selected and used for all the proceeding training and accuracy measurements.

The cost and gamma cross validation is processor-intensive, taking multiple days if executed in a serial fashion. However, since each test is independently calculated it easily lends itself to parallelization. A parallelized version was implemented, running on a modern quad core processor with two virtualized cores per physical core (for a total of four physical and eight virtualized cores) resulting in a reduction in processing time by a factor of five. This reduced the processing time down to 1-2 days (depending on the sampling parameters) which is quite reasonable as it only needs to be performed once per cohort of subjects for a particular disease or image type. If the work load were further divided between more cores or more computers it could be reduced further.

Once the cost and gamma parameters were selected, the computation time was minimal. The classifier must be trained using the selected parameters but this takes less than a minute and only needs to be performed once per cohort of subjects. Once the classifier has been setup classifying a single dataset takes less than 10 seconds. The total computation time per dataset for the automated section (brain extraction, thresholding, and SVM classification) is thus around one minute.

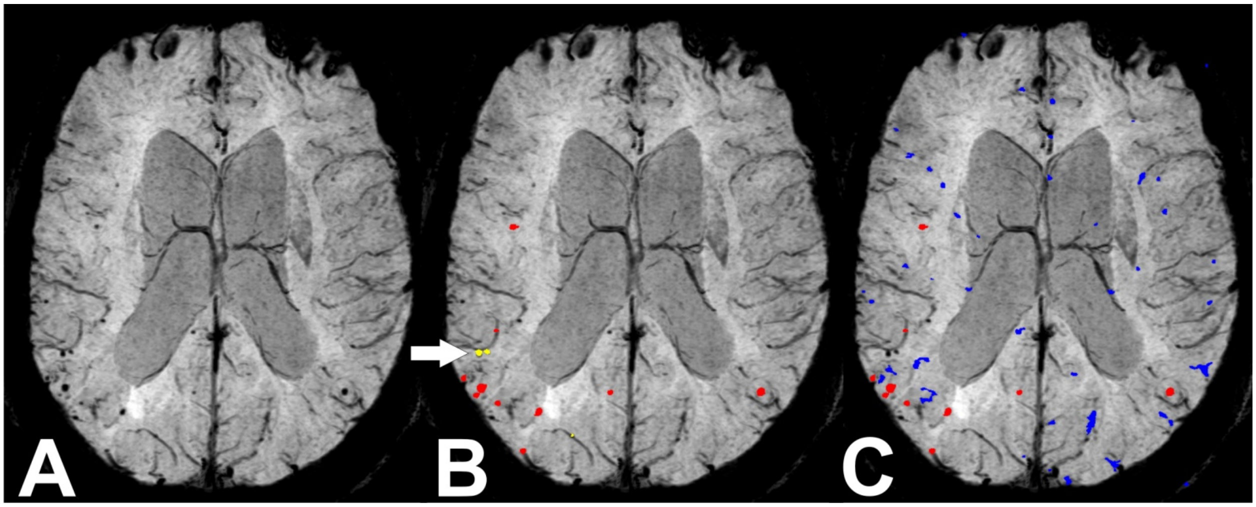

Figure 4.5. A) mIP over 26mm of SWI data. B) Manually marked true CMBs identified using magnitude, phase, SW, and mIP images. C) Automatically marked suspected CMBs. The yellow CMBs (marked by arrows) indicate the ones that were missed by the automated methods, the red indicate bleeds that were identified in both methods, and blue are the false positives from the automated methods. The bleeds that were missed by the automated methods (yellow) were merged with the vein they lie adjacent to causing them to have more vein like features.

Results

Accuracy of the semi-automated technique was evaluated in a binary fashion. If the semi-automated technique identified a cluster of voxels in the final results where a CMB had been identified in the manual review it was considered a true positive, if no cluster of voxels were marked in the final results in that area it was considered a false negative. The issues of edge definition and extraneous surrounding voxels being included in a CMB cluster and contaminating the results practically was not a problem. Clusters that contained both a CMB and surrounding non-CMB voxels were generally eliminated by the classifier as the non-CMB voxels tended to spoil their CMB features (namely shape). All true CMBs that were selected by the classifier had a relatively clean and logical boundary, with a minimal amount of extraneous voxels (Figure 4.5).

The thresholding step had a very high sensitivity of 95%, only missing six CMBs out of 126 (see Table 4.1). However, it had a very large number of false positives as it is designed to mark all hypointense structures in the image. The SVM classifier is able to remove most of the false positives at the loss of some sensitivity. The classifier had an individual sensitivity of 85.8% and specificity of 13.8%. This gives the automated processing an overall sensitivity of 81.7% and specificity of 13.8%. After the data has undergone manual review the remaining false positives are removed for a final sensitivity and specificity of 81.7% and 100% respectively.

	Threshold	SVM Classifier	Manual Review
Total True Positives	120	103	103
Total True Negatives	NA	15,162	15,807
Total False Positives	15,807	645	0
Total False Negatives	6	23	23
Individual False Negatives	6	17	0
Individual Specificity	0.8%	13.8%	100%
Individual Sensitivity	95.2%	85.8%	100%
Combined Specificity	0.8%	13.8%	100%
Combined Sensitivity	95.2%	81.7%	81.7%

Table 4.1. Shows the accuracy of each step in the process. Note the high number of false positives from the thresholding step requires the use of an automated classifier. The classifier eliminates most of the false positive but leaves a significant number (~600). These are spread across six datasets meaning there are approximately 100 identified clusters to review per dataset. Combined and total rows show stats for current step plus previous steps.

Conclusions and Future Directions

Development of the classifier focused on maximizing the sensitivity, even at the cost of specificity. The complicated nature of CMB identification makes a manual review of the automated results necessary so CMB mimics are not included. For the sake of efficiency this review is limited to removal of false positives (as manually searching for missed CMBs would make the automated tools redundant). Since false positives are being manually removed, the only cost of a low sensitivity algorithm is a longer manual review time. False negatives on the other hand can never be recovered. Thus, improving the sensitivity increases the accuracy of the identification while improving the specificity only reduces processing time.

The error rates for each step of the process, shown in Table 3.1, indicate that the step requiring the most improvement is the classifier; it is the main source of the loss of sensitivity. The classifier could be improved with a number of different techniques. New features that give the classifier more information about each marked cluster could improve the accuracy substantially. First attempts with this classifier focused on shape features alone as those were thought to be the most promising. When the intensity features were included they resulted in a 10% improvement in the classifier sensitivity. The addition of other relevant features could give similar improvements. Some possible features to try would be anatomical location and intensity features from other MR sequences.

Anatomical location could be determined automatically by fitting to a standardized brain atlas. This could significantly improve the classification as anatomic location is used as one of the evaluating criteria in manual classification. Intensities from other MR sequences could be used after co-registration of the datasets. For example, if high resolution MR angiography post contrast was performed, the veins and the arteries could be excluded based on their bright signal. While co-registration has been used in similar lesion segmentation problems (Lao et al. 2008) and could be used to remove some CMB mimics (Greenberg et al. 2009), it probably would not result in a dramatic improvement in sensitivity as most of the CMBs are not seen in other MR sequences. Nevertheless, it could be an important step in removing false positives and CMB mimics.

Further improvements could be made to the classifier itself. The addition of AdaBoost for classifier training could improve the quality of the SVM classification (Lao et al. 2008; Morra et al. 2010), and should be an area of future research. Other types of classifiers such as artificial neural networks could also be tried.

While the sensitivity of the technique is a little low, this is probably influenced by the dataset and method of manual review. This dataset was part of a serial study so all patients had at least three time points and some patients had four. For the manual review all four datasets were examined and compared to reach a decision about an individual CMB; this was noted to significantly increase the confidence of identification (Ayaz et al. 2009). While this assuredly improves the ground truth accuracy of the manual method this will somewhat unfairly penalize the semi-automated method as it has less information available because it is only able to use a single time point to make a decision. While these numbers are probably a more accurate measure of its sensitivity for the true number of CMBs, a fair comparison against a manual reviewer who only has access to a single time point would probably show much more favorable numbers.

To get accurate manual counts, multiple people reviewed the data independently and then a consensus was sought on discrepancies between the reviewers. While this does lead to accurate and reliable numbers it is too time consuming for practical application. The average time for one person to process a dataset manually varied depending on scan quality and number of CMBs but can range from 15 minutes to a few hours with most patients taking approximately 30 minutes. This is too time-consuming to be performed clinically—much less two or three times (by multiple reviewers or across multiple time points) to improve consistency. Reviewing a specific list of suspected CMBs generated by semi-automated detection improves consistency and reduces the manual review time to approximately 5 minutes, allowing the data to be efficiently assessed even by multiple reviewers.

Gains in specificity could likely be obtained by using datasets with higher SNR acquired at higher fields (≥3T). The higher SNR would allow α to be set to higher values, excluding more background voxels and reducing false positives. Gains in specificity for the automated portion could further reduce manual review times as fewer false positives would have to be removed manually.

The segmentation techniques and software developed by one of the authors (SB) have also been successfully applied to the related problem of segmenting and quantifying veins in SWI (Ge et al. 2009). This is a simple extension where the shape filtering/classification is run in the other direction and seeks to eliminate more spherical shapes (unwanted dark structures) and keep cylindrical objects (veins). This earlier work used a more simplistic filter (linear thresholds) with only two features (compactness and relative anisotropy). Extending this to use SVM and all 14 features proposed here could improve results significantly.

The training requirements of the classifier need to be explored in more depth. This is by far the most time intensive part of the operation, both in the manual CMB identification that is required for the SVM classifier training and the computational time for cost and gamma parameter selection. Due to this, it is highly desirable to minimize the amount of training that needs to be done, especially across studies. How well the classifier will perform when trained on data collected at one institution or on one type of patients and applied to data from a different institution or a different type of patients remains to be determined. Despite this, even if training is required for each cohort of patients, manually counting a subset of the subjects for training will still require less time than manually counting all of the subjects. Processing times for training can be further reduced using parallelization algorithms (as we implemented) and multi-core multi-processor computers which are becoming increasingly common.

In conclusion we have shown a semi-automated technique of identifying and quantifying CMBs can perform reasonably well with minimal manual intervention. This technique dramatically reduces the processing time and should lead to more consistency between observers. Further verification on a larger group of patients with more diverse types of CMBs needs to be done to prove the applicability of this method as a general CMB detection algorithm.

Role of the funding source

This work was supported by the National Institutes of Health (NIH); Contract grant number: 2R01 HL062983-04A2. They had no role in the study design; in the collection, analysis, and interpretation of data; in the writing of the report; and in the decision to submit the paper for publication.

CHAPTER 5 – THE SETTLING PROPERTIES OF VENOUS BLOOD DEMONSTRATED IN THE PERIPHERAL VASCULATURE USING SWI

Introduction

Deep venous thrombosis (DVT) is a relatively common occurrence in the general population with an incidence of one to three individuals per 1000 per year (Anderson et al. 1991; Nordstrom et al. 1992; Rosendaal 1997; Oger 2000; Cushman et al. 2004). Certain activities and risk factors, such as immobility, can raise this dramatically. A recent study showed that for 2000 DVT patients with age matched spouses the probability of developing DVT after being stationary in a plane, train, or car for more than 4 hours was increased more than 2 fold (Cannegieter et al. 2006). Other types of immobility such as paralysis, bed rest, or even prolonged computer use have also been shown to increase the risk of thrombosis (Homans 1954; Gibbs 1957; Warlow 1978; Beasley et al. 2003). There are many different causes for DVT (Rosendaal 2005) but blood stasis appears to be the most important (Mammen 1992).

The goal of this study was to investigate how blood behaves when the subject is at rest for up to one hour. More specifically, early experiments suggested that blood may actually settle into two components, plasma on the top and red blood cells on the gravitational bottom. Susceptibility weighted imaging (SWI) is a well-established sequence (Haacke et al. 2004; Haacke et al. 2009) that has been shown to produce good venographic images of the brain (Reichenbach et al. 1997; Reichenbach et al. 2000; Koopmans et al. 2008). In this context, it relies on the susceptibility shift caused by deoxyhemoglobin in the venous blood to generate contrast in the phase image. Here, SWI was used to image the veins of the leg and to determine if the red blood cells were settling during blood stasis in the calf. SWI is only sensitive to the deoxyhemoglobin in blood so an increased concentration of red blood cells would cause increased contrast in the phase image. This makes using SWI filtered phase images ideal for imaging blood settling or the early formation of potential clots.

Materials and Methods

A total of 9 healthy subjects were scanned ranging in age from 18-58 years. Scans were performed on a 1.5T Siemens Sonata system with a circularly polarized knee coil. A three dimensional (3D) SWI sequence (fully flow compensated gradient recalled echo) with the following imaging parameters was used: TR = 21ms, TE = 9.95ms, FA = 20°, BW = 190 Hz/pixel, matrix = 384x512x64, resolution = 0.39x0.39x1.6 mm^3, acquisition time = 8 minutes and no parallel imaging. The area of interest was below the knee at the level of the popliteal trifurcation with the volume centered 12 cm below the tibial plateau. The knee was positioned to be slightly bent in the coil. Imaging was performed in the transverse plane. Echo times were chosen to be in-phase to avoid any changes in the phase image from fat. No cardiac gating was performed but a low flip angle was used to create a more spin density weighted image (Haacke et al. 1999). Blood with a constant effective spin density will have little to no pulsatile flow ghosting artifacts.

The echo time was chosen empirically based on results from initial scans, the relatively short TE of 10ms was chosen because longer TEs caused phase aliasing. There is also theoretical backing for this choice. The standard echo time for SWI at 1.5T is chosen to be 40ms for vessels parallel to the field in order to generate a phase shift of nearly π radians (Reichenbach et al. 2000; Haacke et al. 2009). The contrast in the phase images is large enough at TE = 40ms to allow a reduction of the echo time to 10ms and still maintain enough contrast-to-noise to visualize the veins. We are also imaging settled red blood cells which will have approximately 2 to 2.5 times the phase effect as mixed blood (concentration of ≈100% versus ≈40 to 50%). The contrast in the red blood cell region will accordingly be 2 to 2.5 times higher than in the mixed blood situation.

Subjects were entered into the magnet and a transverse SWI scan was completed within 10 minutes of the leg being stationary. Some additional high resolution sagittal scans were performed and then a second transverse SWI scan was performed after the subject had been stationary in the magnet at least 40 minutes to see if any blood settling had occurred. All nine subjects were scanned in the supine position; one of the subjects was taken out of the magnet, allowed to walk around for a brief period, and then rescanned in the prone position to validate the effect of gravity. This subject also had the read and phase encoding gradients swapped while they were in the supine position to ensure that the observed effect was not related to motion or a direction related artefact.

Phase images were examined to see if settling had occurred. A large vein with the most obvious layering was selected from the second time point and regions of interest were manually drawn around the lower and upper layers. A one-tail t-test was used to see if there had been a change in these regions between the first and second time point. Finally, correlation between the size of the bottom layer and both age and vessel size were tested using the Pearson's correlation test.

Results

Generally, a statistically significant decrease in phase only on the gravitational bottom of the vessel was noted in all patients except the youngest (18 years) (Figure 5.4). To guarantee this was a physiological phenomenon we investigated whether or not some MR phenomena might explain the layering. First, we swapped read and phase encoding with no effect: layering was still present. Second, we validated it could be seen in the sagittal scans, although it was easier to observe in the transverse scans. Third, the layering was not closely associated with bifurcations or complicated geometry. Fourth, the effect of gravity was investigated with a volunteer changed from the prone to the supine position. The dark layer was observed to move from the lower to the upper part of the vein showing a clear gravity effect of the layering (Figure 5.1).

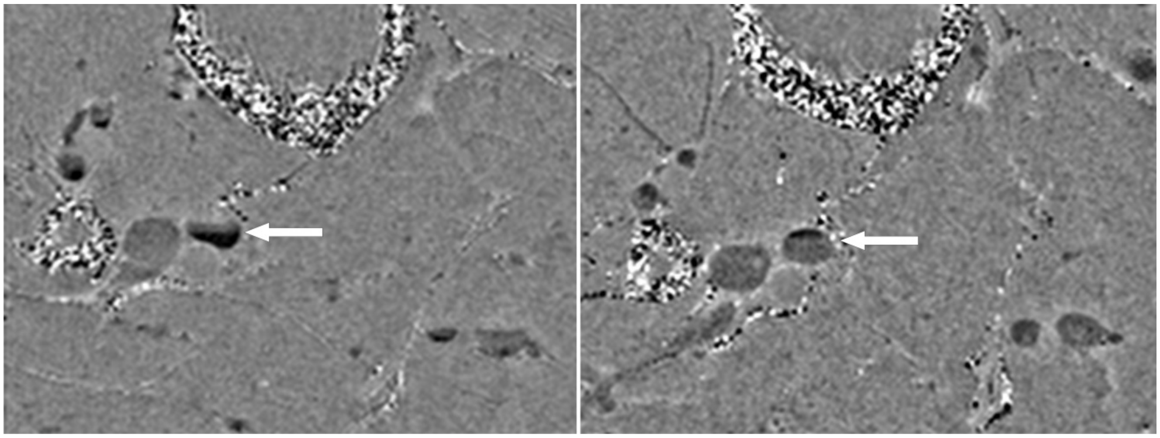

Figure 5.1. The left image shows the subject scanned in the supine position and the right image shows the subject in the prone position. Notice the dark layer switches location from the bottom of the vein to the top mimicking the direction of gravity (lower part on the left and upper part on the right). Male, age 57.

In most subjects the blood was seen to divide into two layers in the phase image, a dark bottom layer of red blood cells and a lighter top layer that appears to be normal mixed blood. In one subject (Figure 5.1, left image) three layers could be observed, a dark bottom layer of red blood cells, a middle layer or what appeared to be the usual mixed blood scenario, and a top layer that was nearly isointense with the background.

The layering was also observed to increase with time spent stationary in the magnet. The early scan (≈10 minutes stationary) showed very little or no layering on all the subjects while the later scan (≈40 minutes stationary) showed increased layering on all the subjects except one subject who didn't show layering until 60 minutes and the youngest subject who never showed layering. Figure 5.2 shows an example of a subject at two time points each with different levels of settling in the major and smaller veins. The larger vessels showed an increase in size of the dark layer at the later time point, up to ≈70% of the vessel, while some of the smaller vessels became completely dark in the later scans.

We also evaluated the distribution of the phase in a major vessel for one subject and this result is shown in Figure 5.3. It can be seen that the broad and roughly Gaussian distribution for the early time point morphs into a bimodal distribution after 40 minutes. The phase values are for a right handed system which gives the standard SWI phase contrast (blood dark), so low phase values in the histograms and bar graphs represent dark regions on the images.

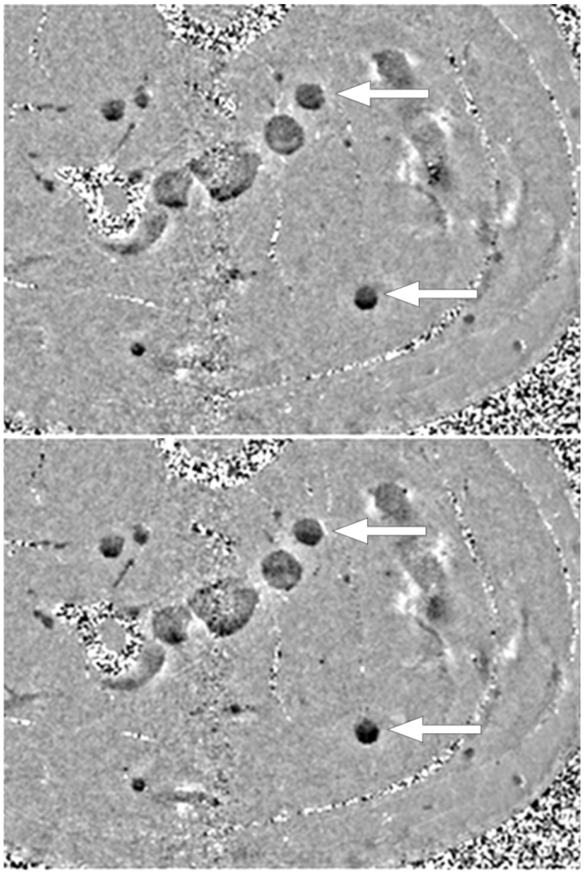

Figure 5.2. Top, early scan (≈10min) and bottom, late scan (≈40min). Notice the vessel towards the bottom; in the early scan the dark layer is about 25% of the vessel and in the late scan the dark layer fills more than 50% of the vessel. Male, age 54.

The amount of layering observed was correlated with the size of the vein (Pearson's correlation p<0.001) with larger veins showing increased layering. Older subjects also tended to have larger veins than younger subjects (including two father son matched pairs) and age was correlated with amount of layering at the one-tailed 95% confidence interval (Pearson's correlation p=0.03). Additional subjects would be needed to improve the statistics. While most of the younger subjects did show a statistically significant phase shift (one-tailed t-test Figure 5.4) the size of the lower layer was usually very small (Figure 5.5) and layering was not seen in multiple veins. Layering was seen to some extent in all subjects except the 18 year old. One other subject (female, 49) did not initially show layering, but after being kept in the magnet an additional 20 minutes (60 minutes total) and rescanned some minor layering in the smaller veins was observed.

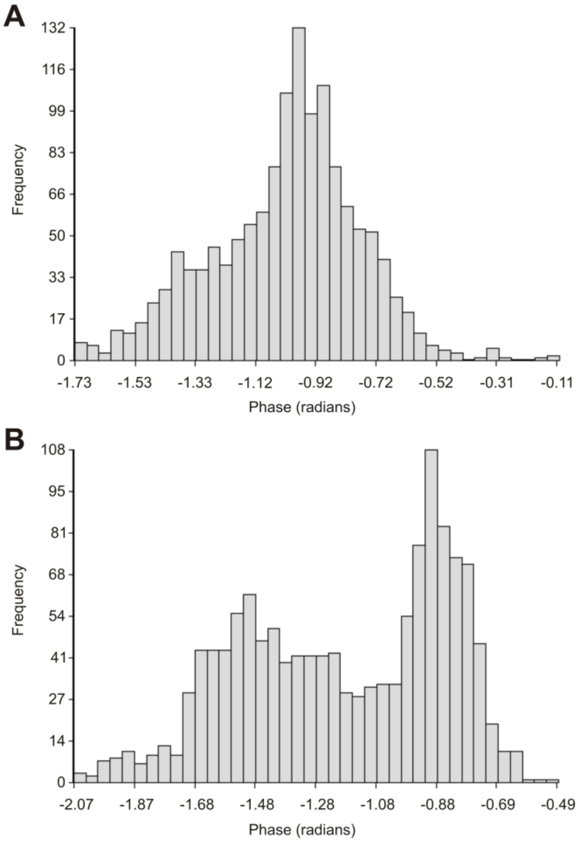

Figure 5.3. Histograms of the phase for a cross section of a large vein after 10 minutes (a) and 40 minutes (b). The top graph shows a Gaussian distribution with a slight broadening of the left shoulder indicating some early layering after 10 minutes. The late scan shows a clear bimodal distribution as two distinct layers have now formed.

This effect was also dependent on the position of the leg. One subject who showed layering with their leg slightly bent (a small support was placed under the knee) was rescanned with the leg completely straight and no layering was observed. This is consistent with the layering being associated with blood stasis and settled blood as lying down with the knees slightly elevated and bent has been shown to increase blood stasis in the leg (Lindstrom et al. 1977).

Discussion

The layering was most reliably correlated with the size of the veins. Smaller veins, typically seen in younger subjects, have faster flow which is most likely why they show less layering. The one older subject that did not initially show layering (female, 49) also had small veins, possibly due to the calf being partially supported and compressed. That the layering should be related to age makes sense as age is one of the strongest risk factors for venous thrombosis. Incidence in the young (<20 years) is very low (1 in 100,000 per year) while incidence in the elderly (>75 years) is almost 1% per year, a thousand fold increase (Rosendaal 1997; Oger 2000; Cushman et al. 2004). The reasons behind this are unclear (Rosendaal 2005), but the increase in venous stasis due to the larger vessels offers a possible explanation.

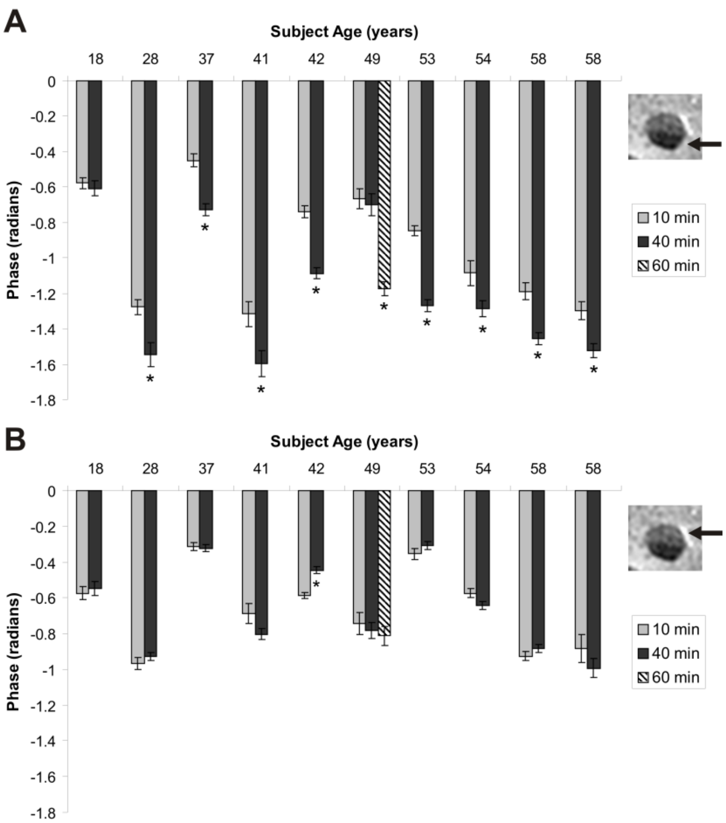

Figure 5.4. Measurements of the phase in the bottom or red blood cell layer (a) and the top or mixed blood layer (b) of a vein at different time points, error bars shown are SEM. In the bottom layer (a) all subjects show a statistical difference (one-tailed t-test * indicates p<0.01) between time points except the 18 year old. The 49 year old showed no difference at 40 min, but when

kept in the magnet and scanned again at 60 min showed a statistical difference. The top layer (b) showed almost no statistical difference between the time points.

The separation of the blood into different layers after less than 40 minutes has major implications. The denser red blood cells appear to sink as the blood flow from certain vessels seems to be reduced and shunted to other vessels. Deoxyhemoglobin in red blood cells is responsible for the phase shift in venous blood, as the cells settle out the increased concentration causes an increased phase shift in the lower layer. The expected phase shift of venous blood assuming well mixed blood with a normal oxygen saturation (Y_0 = 55%) and hematocrit (Hct_0 = 40%) for a vein parallel to the static field at 1.5T is (Chu et al. 1990; Reichenbach et al. 2000):

$$\Delta\phi_{theory}(TE) = -64.3\pi\, {}^{rad}\!/_{\sec\cdot T} \cdot B_0 \cdot (1 - Y_0) \cdot Hct_0 \cdot TE \tag{5.1}$$

$$\Delta\phi_{theory}(TE) = -17.4\pi\, {}^{rad}\!/_{\sec} \cdot TE \tag{5.2}$$

An expression can then be written for the local hematocrit in the lower layer based on the measured and expected phase:

$$Hct_{LL}(\Delta\phi) = \frac{\Delta\phi}{\Delta\phi_{theory}} * \frac{1 - Y_0}{1 - Y} * Hct_0 \tag{5.3}$$

where Y_0 is expected oxygen saturation used in equation 5.2, Y is the actual oxygen saturation, and Hct_0 is the expected hematocrit of mixed blood used in equation 5.2. Alternatively, the theoretical expected phase ($\Delta\phi_{theory}$) could be replaced with a value that is determined experimentally by measuring the phase of a well-mixed vein in which no layering is observed. Substituting $\Delta\phi_{theory}$ for the theoretical value and $\Delta\phi$ for the measured value in the lower layer yields values close to unity when $Y=Y_0$ (mean ± standard error of $Hct_{LL} = 1.00 \pm 0.05$) suggesting that we are indeed imaging settling of the red blood cells where the plasma no longer plays a role.

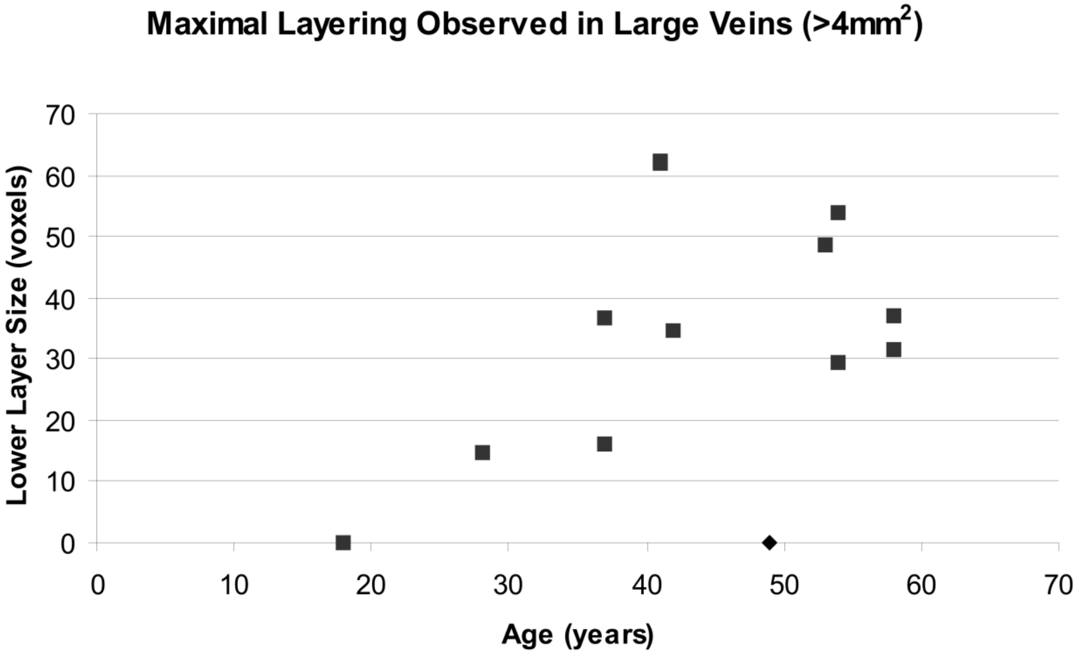

Figure 5.5. Measurements of the amount of layering seen in the large leg veins. The size of the lower layer in a large vein with the most prominent layering was manually measured. With the 49 year old subject excluded the amount of layering was seen to correlate with age with the older subjects showing increased layering (Pearson's correlation p=0.03). The 49 year old subject (diamond) showed no layering at 40 min, then some layering at 60 min but only in a smaller vein (<4 mm^2). The calf of this subject was supported and therefore slightly compressed possibly preventing blood stasis.

In many small veins, and some lager veins, the layer of mixed blood seemed to disappear altogether. This would suggest a buildup of red blood cells and a displacement of mixed blood leading to an increased local hematocrit in that vessel. In the case where three layers were observed (Figure 5.1 left image), the top portion seems to nearly disappear into the background. We suspect this might be pure plasma which has a susceptibility of water similar to other tissues and therefore causes nearly no phase shift.

Correlating the changes in oxygen saturation with flow would also be of interest, but flow in these veins is extremely slow making it difficult to measure. Further, especially in the small veins, very high resolution cardiac gated scanning would be required. Initial attempts at this using phase contrast MRI were unsuccessful, but mapping out the flow effects and correlating them to the changes in phase would be very useful as further research.

This method could potentially be used as a screening procedure to determine a patient’s risk factor for developing a DVT. The increased concentration of red blood cells could increase the likelihood of a clot forming and the layering appears to be correlated with age which is a well-known risk factor for DVT (Mammen 1992; Rosendaal 2005). Much more work needs to be done to resolve this question.

Finally, in the past researchers have used T2* of veins as a means of monitoring oxygen saturation and even noted an inconsistency *in vivo* in these measurements. The results shown here may explain why T2* measurements are so variable in veins since after the blood starts settling the T2* values will change completely from a one compartment mixed blood system to two single compartments of red blood cells and plasma. If the short T2* of the red blood cells is used then the wrong oxygen saturation results will follow.

Conclusions and Future Directions

These hypotheses of blood stasis and blood settling still require verification with independent techniques. This verification could be accomplished in a number of ways. Phase contrast flow quantification in the leg would be very helpful in accomplishing this, especially a full 3D analysis of the flow behavior. The quantified flow measurements could be correlated with the layering to increase the confidence that we are actually imaging blood stasis and settling. The flow measurements could also be performed with ultrasound. While ultrasound is easy to preform, inexpensive, and is the clinical standard for imaging DVT, MR flow measurements make more sense in this instance. The MR flow measurements could be interleaved with the SWI acquisition so there would be no changes from the patient moving or repositioning the leg.

Confirmation could also be obtained with a phantom model system. Animal blood could be used to construct a phantom consisting of tubes of different diameters and varying flow rates.

The fluid dynamics and changes in the blood could then be directly observed in addition to the MR measurements of the system.

Finally, this work offers the possibility of estimating the hematocrit in-vivo (by comparing settled and mixed phase values) and looking at the different fluid dynamics of the settled and mixed layers to better understand DVT formation.

In conclusion, this work has shown a layering effect in the veins of the leg when a subject is at rest for 40 minutes which we postulate is associated with blood stasis and the settling of red blood cells. This could have important implications for understanding the formation of DVT and could possibly be used to assess a patient's risk of DVT. Using SWI filtered phase information offers a new means to study changes in oxygen saturation in subjects at rest for long periods of time.

REFERENCES

Anderson, F. A., Jr., Wheeler, H. B., Goldberg, R. J., Hosmer, D. W., Patwardhan, N. A., Jovanovic, B., Forcier, A. and Dalen, J. E., 1991. A population-based perspective of the hospital incidence and case-fatality rates of deep vein thrombosis and pulmonary embolism. The Worcester DVT Study. Arch Intern Med 151(5): 933-938.

Ayaz, M., Boikov, A. S., Haacke, E. M., Kido, D. K. and Kirsch, W. M., 2009. Imaging cerebral microbleeds using susceptibility weighted imaging: One step toward detecting vascular dementia. J Magn Reson Imaging 31(1): 142-148.

Barnes, S. R. S., 2008. Imaging the small arteries of the brain, M4 and beyond, with MRA. Biomedical Engineering. Detroit, Wayne State University. Masters of Science**:** 75 p.

Barnes, S. R. S., Jin, Z., Du, Y. P. and Deistung, A., 2010. MR Angiography and Venography of the Brain. MRI Susceptibility Weighted Imaging: Basic Concepts and Clinical Applications. E. M. Haacke and Reichenbach, J., Wiley**:** In Press.

Beasley, R., Raymond, N., Hill, S., Nowitz, M. and Hughes, R., 2003. eThrombosis: the 21st century variant of venous thromboembolism associated with immobility. Eur Respir J 21(2): 374-376.

Bosmans, H., Marchal, G., Lukito, G., Yicheng, N., Wilms, G., Laub, G. and Baert, A. L., 1995. Time-of-flight MR angiography of the brain: comparison of acquisition techniques in healthy volunteers. AJR Am J Roentgenol 164(1): 161-167.

Bottomley, P. A., Foster, T. H., Argersinger, R. E. and Pfeifer, L. M., 1984. A review of normal tissue hydrogen NMR relaxation times and relaxation mechanisms from 1-100 MHz: dependence on tissue type, NMR frequency, temperature, species, excision, and age. Med Phys 11(4): 425-448.

Bribiesca, E., 2000. A Measure of Compactness for 3D Shapes. Computers and Mathematics with Applications(40): 1275-1284.

Bullitt, E., Ewend, M., Vredenburgh, J., Friedman, A., Lin, W., Wilber, K., Zeng, D., Aylward, S. R. and Reardon, D., 2009. Computerized assessment of vessel morphological changes during treatment of glioblastoma multiforme: report of a case imaged serially by MRA over four years. Neuroimage 47 Suppl 2: T143-151.

Bullitt, E., Lin, N. U., Smith, J. K., Zeng, D., Winer, E. P., Carey, L. A., Lin, W. and Ewend, M. G., 2007. Blood vessel morphologic changes depicted with MR angiography during treatment of brain metastases: a feasibility study. Radiology 245(3): 824-830.

Cannegieter, S. C., Doggen, C. J., van Houwelingen, H. C. and Rosendaal, F. R., 2006. Travel-related venous thrombosis: results from a large population-based case control study (MEGA study). PLoS Med 3(8): e307.

Chang, C.-C. and Lin, C.-J., 2001. LIBSVM : a library for support vector machines. Software available at http://www.csie.ntu.edu.tw/~cjlin/libsvm.

Chu, S. C., Xu, Y., Balschi, J. A. and Springer, C. S., Jr., 1990. Bulk magnetic susceptibility shifts in NMR studies of compartmentalized samples: use of paramagnetic reagents. Magn Reson Med 13(2): 239-262.

Cordonnier, C., Al-Shahi Salman, R. and Wardlaw, J., 2007. Spontaneous brain microbleeds: systematic review, subgroup analyses and standards for study design and reporting. Brain 130(Pt 8): 1988-2003.

Cordonnier, C., Potter, G. M., Jackson, C. A., Doubal, F., Keir, S., Sudlow, C. L., Wardlaw, J. M. and Al-Shahi Salman, R., 2009. improving interrater agreement about brain microbleeds: development of the Brain Observer MicroBleed Scale (BOMBS). Stroke 40(1): 94-99.

Cushman, M., Tsai, A. W., White, R. H., Heckbert, S. R., Rosamond, W. D., Enright, P. and Folsom, A. R., 2004. Deep vein thrombosis and pulmonary embolism in two cohorts: the longitudinal investigation of thromboembolism etiology. Am J Med 117(1): 19-25.

de Rochefort, L., Liu, T., Kressler, B., Liu, J., Spincemaille, P., Lebon, V., Wu, J. and Wang, Y., 2010. Quantitative susceptibility map reconstruction from MR phase data using bayesian regularization: validation and application to brain imaging. Magn Reson Med 63(1): 194-206.

Deistung, A., Dittrich, E., Sedlacik, J., Rauscher, A. and Reichenbach, J. R., 2009. ToF-SWI: simultaneous time of flight and fully flow compensated susceptibility weighted imaging. J Magn Reson Imaging 29(6): 1478-1484.

Deistung, A., Rauscher, A., Sedlacik, J., Stadler, J., Witoszynskyj, S. and Reichenbach, J. R., 2008. Susceptibility weighted imaging at ultra high magnetic field strengths: theoretical considerations and experimental results. Magn Reson Med 60(5): 1155-1168.

Denk, C. and Rauscher, A., 2010. Susceptibility weighted imaging with multiple echoes. J Magn Reson Imaging 31(1): 185-191.

Du, Y. P. and Jin, Z., 2008. Simultaneous acquisition of MR angiography and venography (MRAV). Magn Reson Med 59(5): 954-958.

Duyn, J. H., van Gelderen, P., Li, T. Q., de Zwart, J. A., Koretsky, A. P. and Fukunaga, M., 2007. High-field MRI of brain cortical substructure based on signal phase. Proc Natl Acad Sci U S A 104(28): 11796-11801.

Fan, Y. H., Zhang, L., Lam, W. W., Mok, V. C. and Wong, K. S., 2003. Cerebral microbleeds as a risk factor for subsequent intracerebral hemorrhages among patients with acute ischemic stroke. Stroke 34(10): 2459-2462.

Fazekas, F., Kleinert, R., Roob, G., Kleinert, G., Kapeller, P., Schmidt, R. and Hartung, H. P., 1999. Histopathologic analysis of foci of signal loss on gradient-echo T2*-weighted MR images in patients with spontaneous intracerebral hemorrhage: evidence of microangiopathy-related microbleeds. AJNR Am J Neuroradiol 20(4): 637-642.

Ge, Y., Zohrabian, V. M., Osa, E. O., Xu, J., Jaggi, H., Herbert, J., Haacke, E. M. and Grossman, R. I., 2009. Diminished visibility of cerebral venous vasculature in multiple sclerosis by susceptibility-weighted imaging at 3.0 Tesla. J Magn Reson Imaging 29(5): 1190-1194.

Gelman, N., Gorell, J. M., Barker, P. B., Savage, R. M., Spickler, E. M., Windham, J. P. and Knight, R. A., 1999. MR imaging of human brain at 3.0 T: preliminary report on transverse relaxation rates and relation to estimated iron content. Radiology 210(3): 759-767.

Gibbs, N. M., 1957. Venous thrombosis of the lower limbs with particular reference to bed-rest. Br J Surg 45(191): 209-236.

Greenberg, S. M., Eng, J. A., Ning, M., Smith, E. E. and Rosand, J., 2004. Hemorrhage burden predicts recurrent intracerebral hemorrhage after lobar hemorrhage. Stroke 35(6): 1415-1420.

Greenberg, S. M., Nandigam, R. N., Delgado, P., Betensky, R. A., Rosand, J., Viswanathan, A., Frosch, M. P. and Smith, E. E., 2009. Microbleeds versus macrobleeds: evidence for distinct entities. Stroke 40(7): 2382-2386.

Greenberg, S. M., Vernooij, M. W., Cordonnier, C., Viswanathan, A., Al-Shahi Salman, R., Warach, S., Launer, L. J., Van Buchem, M. A. and Breteler, M. M., 2009. Cerebral microbleeds: a guide to detection and interpretation. Lancet Neurol 8(2): 165-174.

Haacke, E. M., Brown, R. W., Thompson, M. R. and Venkatesan, R., 1999. Fast Imaging in the Steady State. Magnetic resonance imaging: physical principles and sequence design. New York, Wiley**:** 451-512.

Haacke, E. M. and Lenz, G. W., 1987. Improving MR image quality in the presence of motion by using rephasing gradients. AJR Am J Roentgenol 148(6): 1251-1258.

Haacke, E. M., Miao, Y. W., Liu, M., Habib, C. A., Liu, T., Yang, Z., Lang, Z., Hu, J. and Wu, J., 2010. Correlation of putative iron content as represented by changes in R2* and phase with age in deep gray matter of healthy adults. J Magn Reson Imaging In Press.

Haacke, E. M., Mittal, S., Wu, Z., Neelavalli, J. and Cheng, Y. C., 2009. Susceptibility-weighted imaging: technical aspects and clinical applications, part 1. AJNR Am J Neuroradiol 30(1): 19-30.

Haacke, E. M., Xu, Y., Cheng, Y. C. and Reichenbach, J. R., 2004. Susceptibility weighted imaging (SWI). Magn Reson Med 52(3): 612-618.

Homans, J., 1954. Thrombosis of the deep leg veins due to prolonged sitting. N Engl J Med 250(4): 148-149.

Hsu, C.-W., Chang, C.-C. and Lin, C.-J., 2003 A practical guide to support vector classification. Technical Report.

Imaizumi, T., Horita, Y., Hashimoto, Y. and Niwa, J., 2004. Dotlike hemosiderin spots on T2*-weighted magnetic resonance imaging as a predictor of stroke recurrence: a prospective study. J Neurosurg 101(6): 915-920.

Jezzard, P., Duewell, S. and Balaban, R. S., 1996. MR relaxation times in human brain: measurement at 4 T. Radiology 199(3): 773-779.

Jin, Z., Xia, L. and Du, Y. P., 2008. Reduction of artifacts in susceptibility-weighted MR venography of the brain. J Magn Reson Imaging 28(2): 327-333.

Kirsch, W., McAuley, G., Holshouser, B., Petersen, F., Ayaz, M., Vinters, H. V., Dickson, C., Haacke, E. M., Britt Iii, W., Larsen, J., Kim, I., Mueller, C., Schrag, M. and Kido, D., 2009. Serial Susceptibility Weighted MRI Measures Brain Iron and Microbleeds in Dementia. J Alzheimers Dis 17(3): 599-609.

Koopmans, P. J., Manniesing, R., Niessen, W. J., Viergever, M. A. and Barth, M., 2008. MR venography of the human brain using susceptibility weighted imaging at very high field strength. MAGMA 21(1-2): 149-158.

Lao, Z., Shen, D., Liu, D., Jawad, A. F., Melhem, E. R., Launer, L. J., Bryan, R. N. and Davatzikos, C., 2008. Computer-assisted segmentation of white matter lesions in 3D MR images using support vector machine. Acad Radiol 15(3): 300-313.

Lee, J. H., Sherlock, S. P., Terashima, M., Kosuge, H., Suzuki, Y., Goodwin, A., Robinson, J., Seo, W. S., Liu, Z., Luong, R., McConnell, M. V., Nishimura, D. G. and Dai, H., 2009. High-contrast in vivo visualization of microvessels using novel FeCo/GC magnetic nanocrystals. Magn Reson Med 62(6): 1497-1509.

Lin, W., Mukherjee, P., An, H., Yu, Y., Wang, Y., Vo, K., Lee, B., Kido, D. and Haacke, E. M., 1999. Improving high-resolution MR bold venographic imaging using a T1 reducing contrast agent. J Magn Reson Imaging 10(2): 118-123.

Lindstrom, B., Ahlman, H., Jonsson, O., Sivertsson, R. and Stenqvist, O., 1977. Blood flow in the calves during surgery. Acta Chir Scand 143(6): 335-339.

Mammen, E. F., 1992. Pathogenesis of venous thrombosis. Chest 102(6 Suppl): 640S-644S.

Mittal, S., Wu, Z., Neelavalli, J. and Haacke, E. M., 2009. Susceptibility-Weighted Imaging: Technical Aspects and Clinical Applications, Part 2. AJNR Am J Neuroradiol.

Morra, J. H., Tu, Z., Apostolova, L. G., Green, A. E., Toga, A. W. and Thompson, P. M., 2010. Comparison of AdaBoost and support vector machines for detecting Alzheimer's disease through automated hippocampal segmentation. IEEE Trans Med Imaging 29(1): 30-43.

Nandigam, R. N., Viswanathan, A., Delgado, P., Skehan, M. E., Smith, E. E., Rosand, J., Greenberg, S. M. and Dickerson, B. C., 2009. MR imaging detection of cerebral microbleeds: effect of susceptibility-weighted imaging, section thickness, and field strength. AJNR Am J Neuroradiol 30(2): 338-343.

Nayler, G. L., Firmin, D. N. and Longmore, D. B., 1986. Blood flow imaging by cine magnetic resonance. J Comput Assist Tomogr 10(5): 715-722.

Neelavalli, J., Cheng, Y. C., Jiang, J. and Haacke, E. M., 2009. Removing background phase variations in susceptibility-weighted imaging using a fast, forward-field calculation. J Magn Reson Imaging 29(4): 937-948.

Nishimura, D. G., Macovski, A. and Pauly, J. M., 1986. Magnetic resonance angiography. IEEE Trans Med Imaging 5(3): 140-151.

Nordstrom, M., Lindblad, B., Bergqvist, D. and Kjellstrom, T., 1992. A prospective study of the incidence of deep-vein thrombosis within a defined urban population. J Intern Med 232(2): 155-160.

Oger, E., 2000. Incidence of venous thromboembolism: a community-based study in Western France. EPI-GETBP Study Group. Groupe d'Etude de la Thrombose de Bretagne Occidentale. Thromb Haemost 83(5): 657-660.

Pandian, D. S., Ciulla, C., Haacke, E. M., Jiang, J. and Ayaz, M., 2008. Complex threshold method for identifying pixels that contain predominantly noise in magnetic resonance images. J Magn Reson Imaging 28(3): 727-735.

Park, S. H., Moon, C. H. and Bae, K. T., 2009. Compatible dual-echo arteriovenography (CODEA) using an echo-specific K-space reordering scheme. Magn Reson Med 61(4): 767-774.

Peters, A. M., Brookes, M. J., Hoogenraad, F. G., Gowland, P. A., Francis, S. T., Morris, P. G. and Bowtell, R., 2007. T2* measurements in human brain at 1.5, 3 and 7 T. Magn Reson Imaging 25(6): 748-753.

Potchen, E. J., Haacke, E. M., Siebert, J. E. and Gottschalk, A. 1993. Magnetic resonance angiography: concepts & applications.

Rauscher, A., Barth, M., Reichenbach, J. R., Stollberger, R. and Moser, E., 2003. Automated unwrapping of MR phase images applied to BOLD MR-venography at 3 Tesla. J Magn Reson Imaging 18(2): 175-180.

Reichenbach, J. R., Barth, M., Haacke, E. M., Klarhofer, M., Kaiser, W. A. and Moser, E., 2000. High-resolution MR venography at 3.0 Tesla. J Comput Assist Tomogr 24(6): 949-957.

Reichenbach, J. R., Venkatesan, R., Schillinger, D. J., Kido, D. K. and Haacke, E. M., 1997. Small vessels in the human brain: MR venography with deoxyhemoglobin as an intrinsic contrast agent. Radiology 204(1): 272-277.

Reichenbach, J. R., Venkatesan, R., Yablonskiy, D. A., Thompson, M. R., Lai, S. and Haacke, E. M., 1997. Theory and application of static field inhomogeneity effects in gradient-echo imaging. J Magn Reson Imaging 7(2): 266-279.

Rosendaal, F. R., 1997. Thrombosis in the young: epidemiology and risk factors. A focus on venous thrombosis. Thromb Haemost 78(1): 1-6.

Rosendaal, F. R., 2005. Venous thrombosis: the role of genes, environment, and behavior. Hematology Am Soc Hematol Educ Program: 1-12.

Schrag, M., McAuley, G., Pomakian, J., Jiffry, A., Tung, S., Mueller, C., Vinters, H. V., Haacke, E. M., Holshouser, B., Kido, D. and Kirsch, W. M., 2009. Correlation of hypointensities in susceptibility-weighted images to tissue histology in dementia patients with cerebral amyloid angiopathy: a postmortem MRI study. Acta Neuropathol.

Singh, A. V. and Zamboni, P., 2009. Anomalous venous blood flow and iron deposition in multiple sclerosis. J Cereb Blood Flow Metab 29(12): 1867-1878.

Stanisz, G. J., Odrobina, E. E., Pun, J., Escaravage, M., Graham, S. J., Bronskill, M. J. and Henkelman, R. M., 2005. T1, T2 relaxation and magnetization transfer in tissue at 3T. Magn Reson Med 54(3): 507-512.

Tong, K. A., Ashwal, S., Holshouser, B. A., Shutter, L. A., Herigault, G., Haacke, E. M. and Kido, D. K., 2003. Hemorrhagic shearing lesions in children and adolescents with posttraumatic diffuse axonal injury: improved detection and initial results. Radiology 227(2): 332-339.

Vapnik, V., 1998. Statistical Learning Theory. New York, Wiley-Interscience.

Warlow, C., 1978. Venous thromboembolism after stroke. Am Heart J 96(3): 283-285.

Wasserman, L., 2004. All of statistics : a concise course in statistical inference. New York, Springer.

Xu, Y. and Haacke, E. M., 2006. The role of voxel aspect ratio in determining apparent vascular phase behavior in susceptibility weighted imaging. Magn Reson Imaging 24(2): 155-160.

Xu, Y. and Haacke, E. M., 2008. An iterative reconstruction technique for geometric distortion-corrected segmented echo-planar imaging. Magn Reson Imaging 26(10): 1406-1414.

ABSTRACT

IMAGING THE VASCULATURE WITH SUSCEPTIBILITY WEIGHTED IMAGING: APPLICATIONS AND ANALYSIS

by

SAMUEL RYAN STURGILL BARNES

AUGUST 2010

Advisor: Dr. E. Mark Haacke

Major: Biomedical Engineering

Degree: Doctor of Philosophy

Modern magnetic resonance imaging sequences allow detailed non-invasive imaging of both the arteries and veins. This work is divided into four sections that examine different applications and analysis of these sequences.

Susceptibility weighted imaging (SWI) typically generates excellent negative venous contrast. Techniques to generate positive arterial contrast in SWI images without degrading the venous contrast with a single echo are examined. By using high isotropic resolution and high readout bandwidth, flow losses can be minimized (generating good arterial contrast) even at the long echo times required for good venous contrast. A downsampling filter is then used to restore lost venous phase contrast caused by isotropic resolution. Using these techniques good arterial contrast distal to the middle cerebral artery (MCA) and good venous contrast can be obtained from a single SWI scan.

Traditional magnetic resonance angiography (MRA) is unable to image arteries smaller than approximately 500 µm. The role of flip angle, echo time, image subtraction, and resolution were examined to increase contrast and make much smaller arteries in the 100-200 µm range visible. While hints of these vessels appear, calculations based on current optimized signal levels show that a resolution of 100 µm is required to reliably visualize 100 µm arteries.

Currently these resolutions are not attainable with clinical human scanners limiting our ability to image smaller vessels.

Cerebral microbleeds (CMB) are increasingly being recognized as an important biomarker for other neurovascular diseases. A technique is presented that semi-automatically identifies CMBs in SWI. This will both reduce the processing time and increase the consistency over manual methods. This technique relies on a statistical thresholding algorithm to identify hypointensities within the image. A support vector machine (SVM) supervised learning classifier is then used to separate true CMB from other marked hypointensities. The classifier relies on identifying features such as shape and signal intensity to identify true CMBs. The results from the automated section are then subject to manual review to remove false positives. This technique is able to achieve a sensitivity of 81.7% compared to the gold standard of manual review and consensus by multiple reviewers. This presents a much faster alternative to current manual techniques at the cost of some lost sensitivity.

In the final point of this thesis, the settling properties of venous blood in the peripheral vasculature during periods of immobility were examined. SWI images were collected for nine subjects at two time points: within ten minutes of entering the magnet and after 40 minutes spent stationary in the magnet. Changes in the phase and in the distribution of phase of the veins were used to draw conclusions about the separation of red blood cells from plasma over time. Settling was observed to occur in eight of the nine subjects, the only exception being the youngest subject (18 years). The bottom half of some veins were seen to darken while the top half showed little change often with a clear dividing line between the two. Phase values measured in the bottom layer were consistent with the layer consisting entirely of red blood cells. Settling was seen to increase with time spent stationary and to correlate with the size of veins in the calf. Older subjects tended to have larger veins and consequently more settling of the red blood cells. Our results show that even 40 minutes of rest can easily lead to settling of the blood depending on the position of the leg.

SWI has proven to be a valuable tool to study the venous vasculature, cerebral microbleeds and vessel wall. The work reported here shows the potential of SWI in each of these directions and opens the door for continued development in the study of both the anatomy and function of the vasculature in the body.

AUTOBIOGRAPHICAL STATEMENT

Samuel Barnes was born and grew up in Northern California. He attended Walla Walla University in Washington, taking one year off to study Spanish at Universidad Adventista del Plata in Argentina. He received a B.S. in Electrical Engineering from Walla Walla in 2005. In 2006, he started at Wayne State University studying Biomedical Engineering with a focus on Magnetic Resonance Imaging and received a Master of Science in 2008.